JGR Solid Earth

RESEARCH ARTICLE
10.1029/2022JB025310

In-Situ V_p/V_s Reveals Fault-Zone Material Variation at the Westernmost Gofar Transform Fault, East Pacific Rise

Tianze Liu[1], Jianhua Gong[1], Wenyuan Fan[1], and Guoqing Lin[2]

[1]Institute of Geophysics and Planetary Physics, Scripps Institution of Oceanography, University of California, San Diego, La Jolla, CA, USA, [2]Department of Marine Geosciences, Rosenstiel School of Marine, Atmospheric, and Earth Science, University of Miami, Coral Gables, FL, USA

Key Points:

- Rupture barrier zone has a moderate V_p/V_s of 1.75–1.80
- Down-dip edge of the 2008 M6 mainshock has a low V_p/V_s of 1.61–1.69
- V_p/V_s in the rupture barrier zone increased in the 9 months before the mainshock

Supporting Information:

Supporting Information may be found in the online version of this article.

Correspondence to:

T. Liu,
tianzeliu@ucsd.edu

Citation:

Liu, T., Gong, J., Fan, W., & Lin, G. (2023). In-situ V_p/V_s reveals fault-zone material variation at the westernmost Gofar transform fault, East Pacific Rise. *Journal of Geophysical Research: Solid Earth*, *128*, e2022JB025310. https://doi.org/10.1029/2022JB025310

Received 31 JUL 2022
Accepted 5 MAR 2023

Author Contributions:

Conceptualization: Wenyuan Fan
Data curation: Jianhua Gong
Formal analysis: Tianze Liu
Investigation: Tianze Liu
Methodology: Tianze Liu, Wenyuan Fan, Guoqing Lin
Project Administration: Wenyuan Fan
Software: Tianze Liu
Supervision: Wenyuan Fan
Validation: Tianze Liu
Writing – original draft: Tianze Liu
Writing – review & editing: Tianze Liu, Jianhua Gong, Wenyuan Fan, Guoqing Lin

Abstract Ocean transform faults often generate characteristic earthquakes that repeatedly rupture the same fault patches. The westernmost Gofar transform fault quasi-periodically hosts ~*M*6 earthquakes every ~5 years, and microseismicity suggests that the fault is segmented into five distinct zones, including a rupture barrier zone that may have modulated the rupture of adjacent *M*6 earthquakes. However, the relationship between the systematic slip behavior of the Gofar fault and the fault material properties is still poorly known. Specifically, the role of pore fluids in regulating the slip of the Gofar fault is unclear. Here, we use differential travel times between nearby earthquakes to estimate the in-situ V_p/V_s of the fault-zone materials. We apply this technique to the dataset collected by an ocean-bottom-seismometer network deployed around the Gofar fault in 2008, which recorded abundant microearthquakes, and find a moderate V_p/V_s of 1.75–1.80 in the rupture barrier zone and a low V_p/V_s of 1.61–1.69 in the down-dip edge of the 2008 *M*6 rupture zone. This lateral variation in V_p/V_s may be caused by both pore fluids and chemical alteration. We also find a 5%–10% increase in V_p/V_s in the barrier zone during the 9 months before the mainshock. This increase may have been caused by fluid migrations or slip transients in the barrier zone.

Plain Language Summary Oceanic transform faults are ideal natural laboratories for studying earthquake physics due to their regular behaviors. The westernmost Gofar transform fault near the East Pacific Rise generates magnitude six earthquakes every 5–6 years on two rupture zones, respectively, which are separated by a barrier zone repeatedly stopping ruptures on the adjacent segments. The distinct behavior of the barrier zone might be due to differences in material properties from the rupture zones. To explore this hypothesis, we analyze thousands of small earthquakes in 2008 and find that the barrier zone has a higher ratio between P and S velocities than the rupture zone. This difference indicates that the barrier and rupture zones differ in their fluid content and chemical composition, which may have regulated their distinct slip behaviors. We also find an increase in the ratio between P and S velocities in the barrier zone during the 9 months before the magnitude six earthquake in 2008, which may reflect fluid flows or aseismic fault slips. Our findings suggest that pore fluids and the chemical composition of fault-zone materials likely play a crucial role in regulating the slip behaviors of oceanic transform faults.

1. Introduction

Oceanic transform faults demonstrate some of the most systematic and predictable slip behaviors. Moderate-to large-magnitude characteristic earthquakes often rupture the same fault patches quasi-periodically, which are frequently preceded by systematic foreshock activity (McGuire et al., 2005). This clear earthquake-cycle pattern implies that the underlying physical processes are likely repeatable. Therefore, oceanic transform faults are ideal natural laboratories for studying the mechanisms of earthquake nucleation and arrest (Boettcher & McGuire, 2009; McGuire, 2008). Specifically, their regular cycles provide opportunities to capture anticipated characteristic events and record variations in material properties that may reflect the stress and strength evolution leading to the characteristic earthquakes.

The Gofar transform-fault system at the East Pacific Rise (Figure 1a) exemplifies such regular earthquake behaviors. The fault system has two short intra-transform spreading centers (ITSC) and three segments with the westernmost segment denoted as G3. The G3 segment, situated between the East Pacific Rise (EPR) in the west and an ITSC in the east (Figure 1a), regularly hosts ~*M*6 events every ~5 years at two separate asperities (McGuire, 2008). The two asperities are locked interseismically and are connected by a ~10 km long rupture barrier zone (hereafter

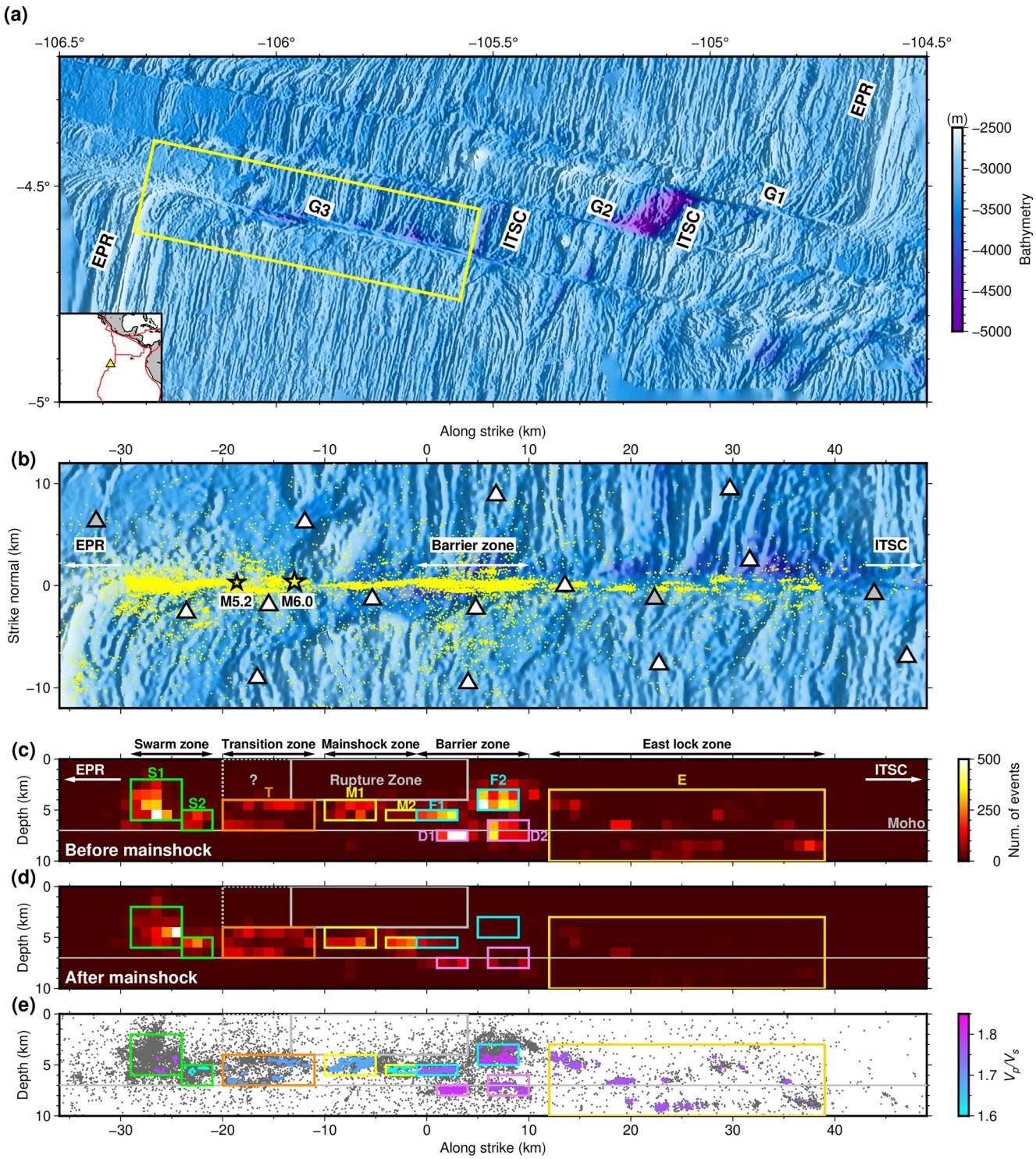

Figure 1.

"barrier zone") along strike. The barrier zone seems to have repeatedly stopped the ruptures of *M*6 earthquakes at the locked zones, including the 18 Sep 2008 *M*6 mainshock that occurred west of the barrier zone (Figures 1a–1c; McGuire et al., 2012). The barrier zone is likely a highly fractured damage zone with a fluid-filled porosity up to 8% and has a ~10%–20% P-wave velocity reduction extending through the whole crust to the uppermost mantle, in contrast to the velocity structure of the rupture zone (Froment et al., 2014; Roland et al., 2012). The average

S-wave velocity of the barrier zone decreased by about 3% and then fully recovered within 1 week prior to the 2008 *M*6 mainshock, showing a dynamic evolution of the material properties (Froment et al., 2014; McGuire et al., 2012). The observed velocity changes are likely related to adjustments of poroelastic properties (e.g., fluid fraction, pore pressure, and pore geometry) resulting from stress changes (McGuire et al., 2012). However, details of the along-strike material-property changes remain elusive primarily due to the limited spatial resolution of conventional imaging techniques.

Rock V_p/V_s is sensitive to both the pore fluids and the mineral composition (Christensen, 1984, 1996; Takei, 2002). Specifically, in-situ V_p/V_s obtained from differential P and S arrival times of nearby earthquakes are capable of resolving fault-zone material properties with high spatial and temporal resolutions in the near-source regions than conventional tomographic images (Bachura & Fischer, 2016; Bloch et al., 2018; Dahm & Fischer, 2014; Lin et al., 2015; Lin & Shearer, 2007, 2009, 2021). For example, Lin et al. (2022) showed that the spatial pattern of the high-resolution in-situ V_p/V_s is much more complex than the tomographic V_p/V_s models in California and that the in-situ V_p/V_s illuminates the important role of fluids in driving repeating earthquakes.

Here, we use an 1-year ocean-bottom-seismometer (OBS) dataset recorded by a 2008 experiment at G3, which captured the anticipated *M*6 characteristic earthquake as well as ∼30,000 microearthquakes, to investigate the variation of in-situ V_p/V_s in the fault zone. We design a new method to examine the spatiotemporal evolution of the in-situ V_p/V_s and validate the method with a suite of synthetic tests. We then compare the estimates with predictions from rock-physics models to infer physical processes within the G3 fault zone.

2. Data

We use the data collected by the 2008 Quebrada-Discovery-Gofar marine seismic experiment (Froment et al., 2014; Gong et al., 2022; McGuire et al., 2012; Roland et al., 2012; Wolfson-Schwehr et al., 2014). The experiment deployed 16 broadband seismographs around G3 (triangles in Figure 1a). Among the 16 stations, three did not record useful data (gray triangles in Figure 1a), and thus our analysis focuses on the waveforms from the rest 13 stations, which were configured to sample at either 50 Hz or 100 Hz. We use the relocation catalog from Gong and Fan (2022) to estimate the in-situ V_p/V_s of the G3 fault zone. The catalog includes both automated and manually determined locations, and we focus on the 30,854 earthquakes reported in the automated catalog in this study (see Gong and Fan (2022) for details). The earthquakes are mostly within ±1 km in the strike-normal direction (Figure 1a). We first obtain both P and S waveforms of the earthquakes, resample the waveforms to 100 Hz, and then bandpass filter the records at 4–20 Hz. The waveforms are windowed from −0.4 to 0.6 s around the predicted P arrivals and −0.8 to 0.7 s around the predicted S arrivals. The predicted P and S arrivals are obtained using a one-dimensional (1D) velocity model extracted from Roland et al. (2012). We cross-correlate the P and S waveforms of each earthquake with those of its closest 100 neighboring events recorded at the same station. The differential P and S travel times and cross-correlation coefficients are computed for each event pair at every available station, but they are only recorded when the cross-correlation coefficients of at least one phase are greater than 0.6. We only keep cross-correlation measurements of an event pair if more than five stations meet the requirement. In total, we obtain 8,857,302 pairs of P and S differential travel times for estimating in-situ V_p/V_s.

3. Methods

3.1. Fault Patches of Interest

The ∼30,000 microearthquakes are nonuniformly distributed within the G3 fault zone. To study the variation of the in-situ V_p/V_s of the G3 fault zone, we focus on ten non-overlapping patches. The selection is primarily guided

Figure 1. Summary of the regional tectonics, observational geometry, and V_p/V_s estimates for the fault patches at the westernmost Gofar transform fault (G3). (a) Map of the Gofar transform fault system. EPR: East Pacific Rise. ITSC: inter-transform spreading center. Yellow box: area around the G3 segment shown in (b). Inset: Map of the east Pacific showing the location of Gofar (yellow triangle) and the plate boundaries (red lines). (b) Stations (triangles; functional and non-functional ones in white and gray, respectively) and events (yellow dots) around G3. Big and small stars: The *M*6.0 mainshock and its largest aftershock of *M*5.2. The origin of the along-strike axis is approximately the same as the one in Figure 3 of McGuire et al. (2012). (c) Seismicity density on the fault plane before the mainshock, binned with 1 km × 1 km grids. Rectangles with different colors mark the fault patches *S1* and *S2* (green) in the swarm zone, *T* (orange) in the transition zone, *M1* and *M2* (yellow) in the mainshock zone, *F1* and *F2* (cyan) in the shallow barrier zone, *D1* and *D2* (violet) in the deep barrier zone, and *E* (gold) in the east lock zone. Dashed gray rectangle: possible *M*6 rupture area in the transition zone. (d) Similar to (b), but for the events after the mainshock. (e) Average V_p/V_s estimated for the whole observation period for each fault patch. Gray dots: All events in Gong and Fan (2022). Colored dots: Events used for estimating the V_p/V_s, colored by the V_p/V_s of the corresponding fault patches.

by the spatiotemporal evolution of seismicity reported in Gong and Fan (2022). The patches differ in their sizes to match the features of the seismicity evolution and to balance the spatial resolution and the number of differential travel time measurements for each patch (Figures 1b and 1c). Only one V_p/V_s is estimated for each patch for a time period. For example, we divide the barrier zone into four patches due to its active seismicity and complex structure, whereas we group the east lock zone into one single patch because of its low seismicity. Regardless of the fault patch dimension, we only use the differential travel times of event pairs within 2 km to obtain local in-situ V_p/V_s estimates. OBS data often have inaccurate timing because the instrument clocks are unable to synchronize with satellites. Although a linear clock correction was applied to the data when the data was archived, the residual nonlinear clock drift may still bias the results (Gouédard et al., 2014). Therefore, we only use event pairs occurring within 30 days to minimize the effects of the clock drifts. We further evaluate the impacts of the maximum event temporal separation in Section 5.1.1.

The eastern G3 hosted an *M*6 event in 2007 prior to the experiment (approximately Zone 1 in Gong and Fan (2022); McGuire et al. (2012)). Because this fault segment had only 2,487 earthquakes during the observational period, we group them into one patch (Patch *E*; *E* is short for "east"; Figures 4 and 1c). The barrier zone (approximately Zone 2 in Gong and Fan (2022)) includes four patches with two shallow patches *F1* and *F2* (*F* is short for "foreshock") and two deep patches *D1* and *D2* (*D* is short for "deep"), where the seismicity rate was high before the mainshock but largely halted after the mainshock (Figures 1b and 1c). We define two patches *M1* and *M2* (*M* is short for "mainshock") at the down-dip edge of the mainshock rupture zone (approximately Zone 3 in Gong and Fan (2022); the rupture zone is largely quiescent before and after the mainshock), with *M1* being seismically active during the whole observation period and *M2* consisting mostly aftershocks of the 2008 *M*6 earthquake (Figures 1b and 1c). We note that *M2* and *F1* are spatially close but have distinct temporal patterns of seismicity (Gong & Fan, 2022), which implies a possible difference in material properties. The events immediately west of the mainshock zone are grouped into the patch *T* (*T* is short for "transition"; approximately Zone 4 in Gong and Fan (2022)), where a moderate level of seismicity persisted through the observational period (Figures 1b and 1c). The *M*6 mainshock may have also ruptured the area above *T* if the rupture propagated bilaterally (Figures 1b and 1c). Near the East Pacific Rise, the western end of G3 hosted a 2-week-long swarm in December 2008, including two *M*5 earthquakes ("December swarm" in McGuire et al. (2012); approximately Zone 5 in Gong and Fan (2022)). This segment is divided into two patches *S1* and *S2* (*S* is short for "swarm"; Figures 1b and 1c).

3.2. Preprocessing of Differential Travel Times

In an ideal case where events occur in a homogeneous medium (P and S rays share the same path), and the measurements contain no error or noise, the P and S differential travel times of an arbitrary pair of events 1 and 2 recorded at the same station i ($\Delta t^p_{12,i}$ and $\Delta t^s_{12,i}$) lie on a line with zero intercept and a slope equal to the V_p/V_s of the medium:

$$\begin{aligned} \Delta t^p_{12,i} &= t^p_{1,i} - t^p_{2,i} \\ &= \Delta l / V_p, \\ \Delta t^s_{12,i} &= t^s_{1,i} - t^s_{2,i} \\ &= \Delta l / V_s, \\ \Delta t^s_{12,i} &= (V_p/V_s)\Delta t^p_{12,i}, \end{aligned} \tag{1}$$

where $t^p_{1,i}$, $t^p_{2,i}$, $t^s_{1,i}$, and $t^s_{2,i}$, are the observed P and S travel times, and Δl is the path-length difference.

In reality, the origin times of the two events contain errors t^o_1 and t^o_2, respectively, which cause the P and S differential times of each event pair to form a line with a non-zero intercept term related to the origin-time errors (e.g., Figure 5 in Lin and Shearer (2007)):

$$\begin{aligned} \Delta t^p_{12,i} &= \left(t^p_{1,i} - t^p_{2,i}\right) + \left(t^o_1 - t^o_2\right) \\ &= \Delta l / V_p + \Delta t^o_{12}, \\ \Delta t^s_{12,i} &= \left(t^s_{1,i} - t^s_{2,i}\right) + \left(t^o_1 - t^o_2\right) \\ &= \Delta l / V_s + \Delta t^o_{12}, \\ \Delta t^s_{12,i} &= (V_p/V_s)\Delta t^p_{12,i} + (1 - V_p/V_s)\Delta t^o_{12}. \end{aligned} \tag{2}$$

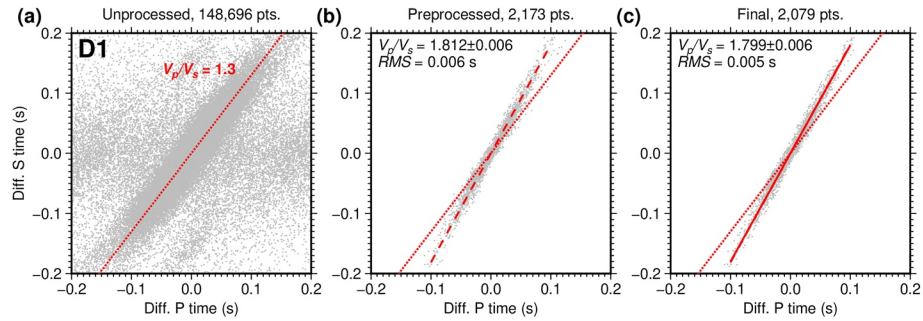

Figure 2. Differential P and S travel times of the *D1* fault patch (Figures 1c–1e) at three data-processing steps. Dotted red lines: Reference line with a slope of 1.3. (a) Unprocessed differential travel times. (b) Differential travel times after preprocessing. (c) Differential travel times used for the final V_p/V_s estimation. Dashed red line: Line with a slope equal to the V_p/V_s estimated using all preprocessed measurements. Solid red line: line with a slope equal to the final V_p/V_s estimate.

Moreover, the differential travel times are computed in an automated fashion, and the measurements might be susceptible to phase misalignment and other sources of random noise, which could potentially bias the in-situ V_p/V_s estimates (see Section 5.1.1 for a detailed discussion). For example, the unprocessed differential travel times for *D1* are highly scattered and suggest a slope of ∼1.3, significantly smaller than the V_p/V_s of typical rocks (Figure 2a). Therefore, we design a preprocessing procedure to reduce the effects of observation errors in differential travel times and select the most robust measurements before estimating in-situ V_p/V_s (Figure 3).

We first remove the arrival-time measurements with a cross-correlation coefficient less than 0.6 for either P or S wave (e.g., Lin et al., 2007). The cross-correlation-coefficient threshold is selected to maximize the number of differential-travel-time measurements for the following quality-control steps while removing obvious outliers. We denote this step by "the CC step" and the following step "the linearity step", which will further select the measurements based on their linear fitting (Figure 3). We then fit a line to the differential travel times of each event while allowing for a non-zero intercept and remove the intercept for the event pair (Figure 3). It is worth emphasizing that our intercept-removing procedure is different from the conventional demeaning method (e.g., Lin & Shearer, 2007). Removing the intercept terms can reduce the effects of event-timing errors while preserving the natural spread of the data points, which is critical in obtaining reliable V_p/V_s estimates and reducing the estimate uncertainties. To assure the robustness of the intercept estimates, we design a quality-control process to determine the data quality of the event pairs (Figure 3). We require a minimum number ($N_{\min}$) of seven data points (each data point represents a pair of P and S differential travel times of two adjacent earthquakes recorded at one station) and keep event pairs with a number of data points greater than the threshold for the following analysis. The threshold is determined as $N_{\min} = 7$ to balance the trade-off between data quality and quantity, and its effect on the in-situ V_p/V_s estimates will be discussed in Section 4.1. We iteratively fit a line for an event pair using the total-least-squares (TLS) regression (also known as "orthogonal-distance regression"; Van Huffel & Vandewalle, 1991), which minimizes the ℓ_2 norm of the misfits for both the P and S differential times. All measurements of an event pair are initially used to estimate a slope and an intercept, and a root-mean-square (RMS) misfit is recorded. If the RMS misfit is below a pre-defined threshold ($RMS_{\max}$), we retain the measurements, remove the associated intercept estimate, and record the slope estimate as the apparent V_p/V_s for this event pair. The apparent V_p/V_s is used in the following steps to determine the data quality of the event pair. Otherwise, we remove the data point having the largest misfit and repeat the line-fitting procedure. This iterative process continues until the RMS misfit is less than $RMS_{\max}$ or the number of measurements of the event pair is less than $N_{\min}$. In the latter case, this event pair will not be used for further analysis. We choose a threshold of $RMS_{\max} = 0.005$ s, a strict criterion given the data sampling interval of 0.01 s. This parameter choice aims to retain only the highest-quality differential travel times for robust estimation. We will also evaluate the effects of different choices of $RMS_{\max}$ in Section 4.1.

We use the joint distribution between the apparent V_p/V_s and differential-P-time ranges (τ) of event pairs to further inspect the measurement quality of each fault patch (Figure 4). The differential-P-time range τ is defined as the difference between the maximum and minimum differential P arrival times ($\tau = \Delta T_{\text{p,max}} - \Delta T_{\text{p,min}}$) for an event pair. For example, Figure 4 shows the joint distributions for *M1* and *D1* after the intercept-removal step. The distributions show measurements forming apparent strips with $V_p/V_s \approx 0$ and $\tau > 0.15$ s (Figure 4), which are clearly erroneous and thus need to be excluded from the analysis. The remaining measurements are distributed

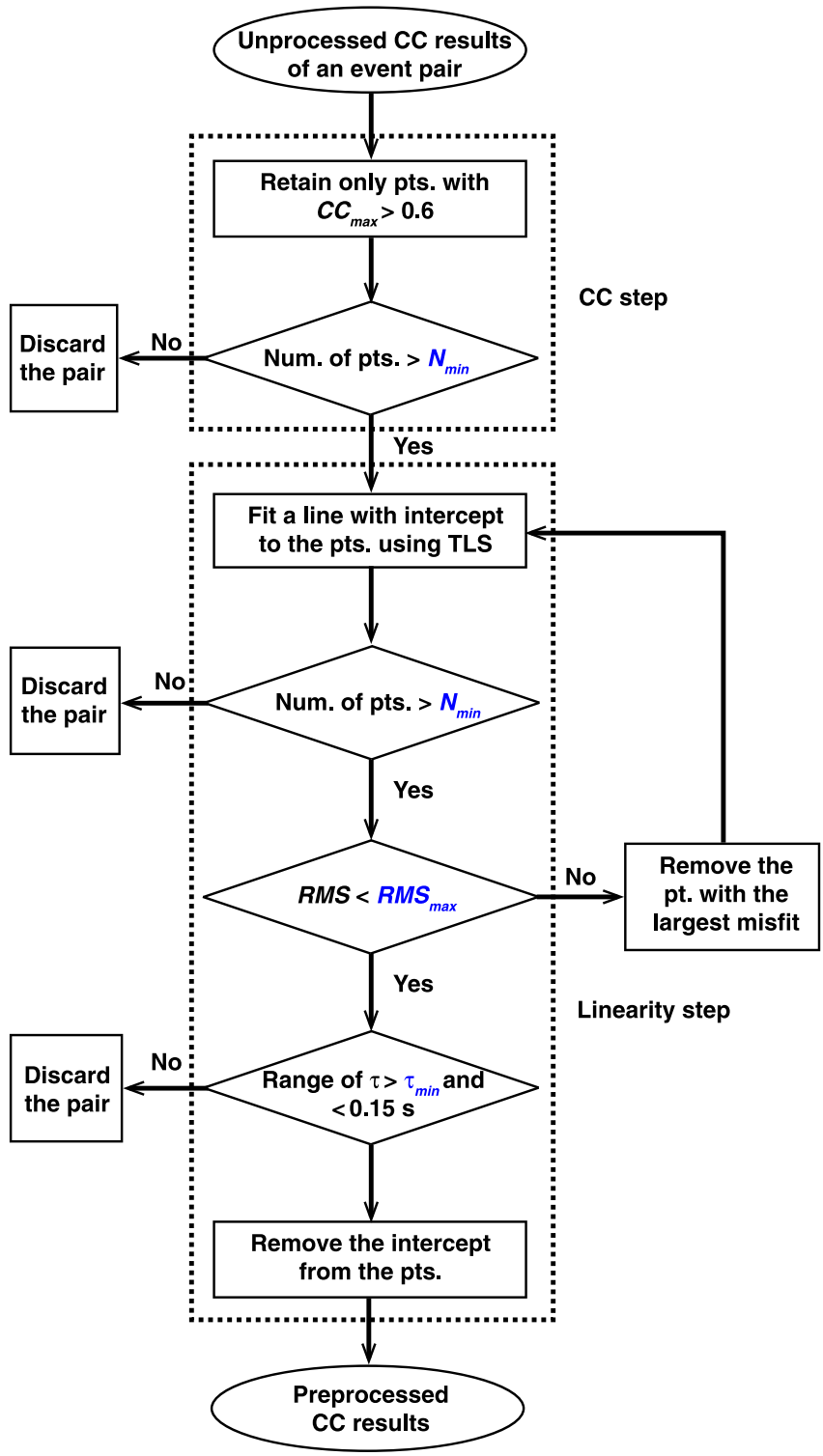

Figure 3. Preprocessing workflow. Key parameters tested in Figure 5 are in blue. TLS: total least squares.

in the ranges of 0.001 s to 0.150 s for τ and 0.5 to 3 for V_p/V_s (Figure 4). This group of measurements is centered around a V_p/V_s of 1.7 and shows a reduction in variation with increasing τ (Figure 4) and thus likely represents the event pairs with reasonable errors. We choose to use event pairs with apparent $V_p/V_s = 0.5$ to 3 and $\tau = 0.050$ s to 0.150 s (solid green boxes in Figure 4) for estimating V_p/V_s. The apparent V_p/V_s range is sufficiently wide

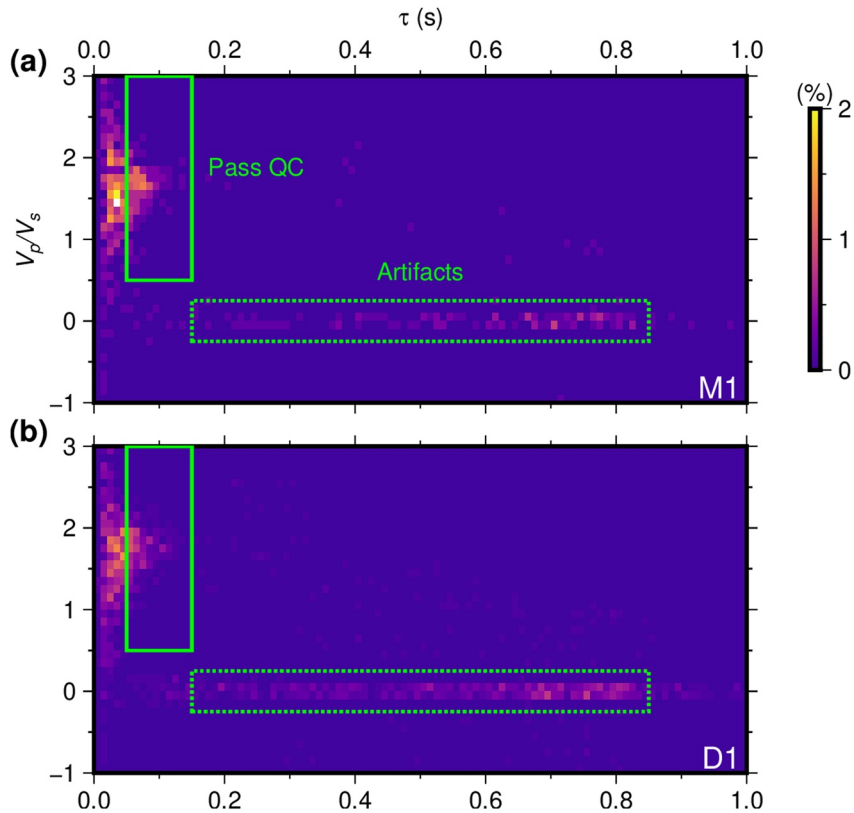

Figure 4. Joint distributions between the apparent V_p/V_s and differential-P-time ranges (τ) of the event pairs with intercept terms removed for (a) *M1* and (b) *D1*. Solid green box: The preferred range for apparent V_p/V_s (0.5–3) and τ (0.05–0.15 s). Dotted green box: A cluster likely consisting of artifacts.

and is centered approximately at the average V_p/V_s of typical rocks (~1.73) to avoid selection bias in choosing the differential travel-time measurements. The lower bound of τ (τ_{min}) is a key parameter because it controls the trade-off between data quantity and quality, and we will discuss its effect in detail in Section 4.1.

The preprocessing procedure removes most of the cross-correlation measurements and retains only a small portion (typically <1%) of the data points. However, the selected measurements have high quality and thus likely yield more accurate estimates. For example, the unprocessed measurements of *D1* produce an unrealistic V_p/V_s estimate of ~1.3, whereas the cleaned measurements yield a best-fitting line with a slope of ~1.8 (Figures 2a and 2b). Elaborate preprocessing could potentially cause selection biases, that is, our strict data-selection procedure could bias the V_p/V_s estimates toward a pre-defined value. However, we emphasize that we use a very wide range (0.5 *to* 3) for the apparent V_p/V_s to minimize biases (Figure 4). We will further test the effects of the preprocessing procedure on synthetic data to confirm the absence of bias in our estimates (Section 5.1.1). Among all fault patches, the swarm-zone patches (*S1* and *S2*) have a remarkably lower fraction of events left for the final V_p/V_s estimation compared to other patches (Figure 1d). Besides, the cleaned measurements in *F2* are mostly located in the deeper part of the patch (Figure 1d). These features may have been caused by the higher degrees of structural complexity (e.g., microfractures) in the swarm and barrier zones. Such structure complexities near the source region could lead to incoherent waveforms between nearby events, causing less reliable differential travel-time measurements. We will further discuss this hypothesis about the data retention rate and structural complexity in Section 5.3.1.

3.3. Robust V_p/V_s Estimation

With the cleaned differential travel times, we estimate the in-situ V_p/V_s for each fault patch following an iterative approach similar to the line-fitting step in the preprocessing procedure. We first fit a line with zero intercept to the measurements and compute the standard deviation of the misfits and remove the measurements with a misfit greater than two times the standard deviation. We then repeat the line-fitting using the remaining measurements

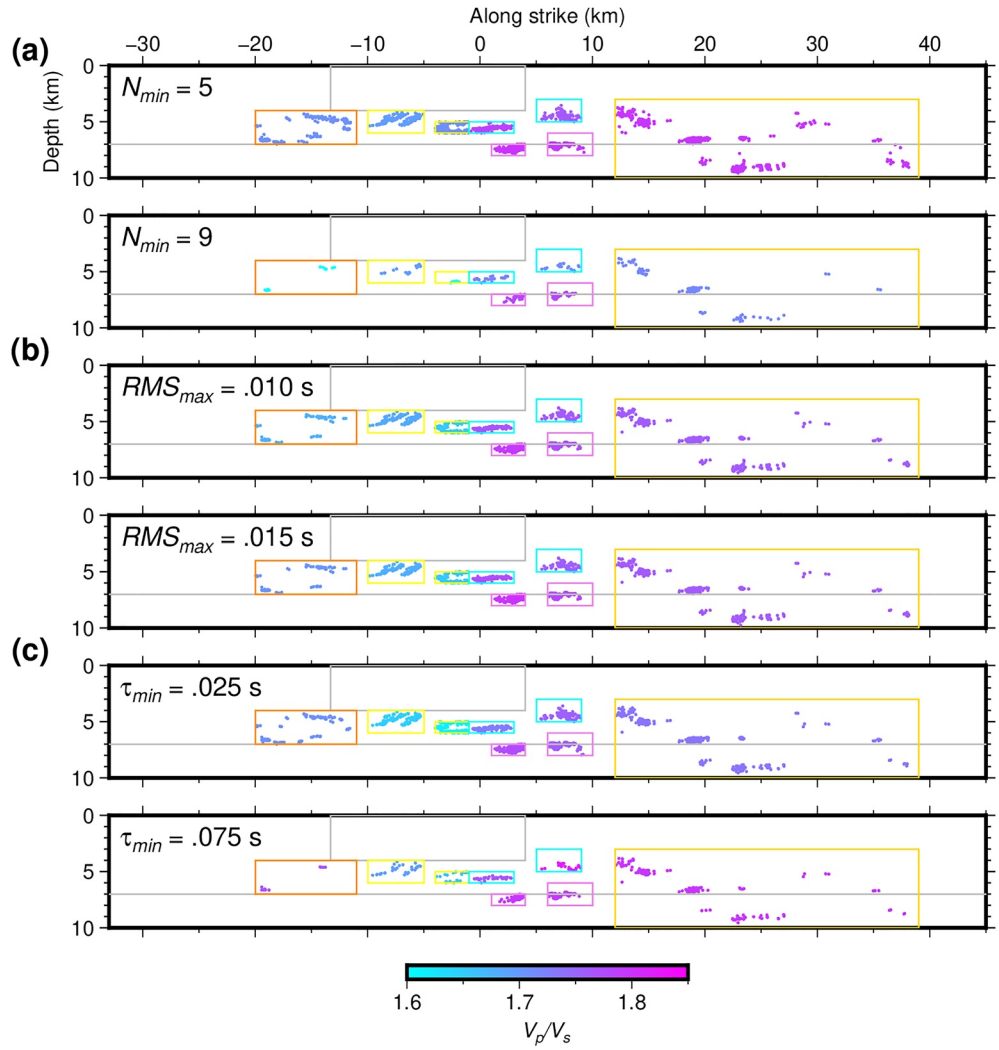

Figure 5. Effects of the three key preprocessing parameters (a) N_{min}, (b) RMS_{max}, and (c) τ_{min} on the spatial pattern of the estimated V_p/V_s. The two accompanying panels show the results of two other parameter choices for (a) N_{min} (5 and 9), (b) RMS_{max} (0.010 and 0.015 s), and (c) τ_{min} (0.025 and 0.075 s) in comparison with the results of the preferred parameter choice shown in Figure 1e. Colored dots and boxes are the same as the ones in Figure 1e.

to obtain the final V_p/V_s estimate. This data removal step typically disqualifies less than 10% of the remaining measurements, and the V_p/V_s estimates are only marginally different between the last two steps (Figures 2b and 2c). We further estimate the uncertainties of the V_p/V_s estimates by computing the standard deviation of the V_p/V_s from 500 bootstrap-resampled datasets. Each bootstrap realization is obtained by randomly drawing the same number of measurements from the original dataset with replacement, allowing the same measurement to be sampled multiple times. Additionally, we also estimate the uncertainties using the jackknife method following Bloch et al. (2018) and find almost identical uncertainties (Table S1 in Supporting Information S2). We thus take the bootstrap uncertainties as the representative values hereafter. We note that the uncertainty estimates from the bootstrap and jackknife methods provide a measure of data variability, which do not directly address uncertainties resulting from choices of preprocessing parameters or the spatial resolution of our data and method (Section 5.1). As an example, the final V_p/V_s for *D1* is estimated to be 1.799 with an uncertainty of ±0.006 and an RMS misfit of 0.005 s. Fig. S1 in Supporting Information S1 shows the data points used for the final V_p/V_s estimation and the corresponding best-fitting models for the other nine fault patches.

4. Results

4.1. Spatial Variation of In-Situ V_p/V_s

The in-situ V_p/V_s estimates of the 10 fault patches show a distinct spatial variation with values ranging from 1.524 to 1.799. The eastern part of G3, including the barrier zone (*F1*, *F2*, *D1*, and *D2*) and the east locked zone (E), has high V_p/V_s(1.752–1.799), whereas the western part, including the mainshock zone (*M1* and *M2*), the transition zone (T), and the eastern patch of the swarm zone (*S2*), has low V_p/V_s (1.524–1.693; Figure 1d). The other fault patch *S1* in the swarm zone has a V_p/V_s value of 1.777, similar to the patches in the east (Figure 1d). Patches *S1* and *S2* have fewer event pairs for estimating V_p/V_s compared to the other patches probably due to the combined effects of poor station coverage and dissimilarity of event waveforms (Figures 1a and 1d). Therefore, the V_p/V_s estimates for *S1* and *S2* are likely less reliable than those of other fault patches and thus will not be further discussed. We observe a sharp contrast in V_p/V_s between the two adjacent patches *M2* and *F1*, which correlates with the temporal variation of their seismicity (Figures 1b–1d; Gong & Fan, 2022). These observations suggest an abrupt boundary in material properties between the mainshock zone and the barrier zone. The in-situ V_p/V_s estimates, their uncertainties, and associated RMS misfits of all fault patches except for *S1* and *S2* are summarized in Table S1 in Supporting Information S2. The estimation uncertainties range between ±0.005 and ±0.013 (Table S1 in Supporting Information S2), which are significantly smaller than the V_p/V_s contrast between the mainshock zone and the barrier zone, confirming the robustness of the observed difference.

To evaluate the robustness of the observed spatial variation, we examine the effects of $N_{\min}$, $RMS_{\max}$, and $\tau_{\min}$ on the V_p/V_s estimates. We test the effects of these parameters by only varying one parameter at a time while keeping the other two at our preferred values of $N_{\min} = 7$, $RMS_{\max} = 0.005$ s, and $\tau_{\min} = 0.05$ s, leading to six additional sets of parameter combinations for the eight fault patches (excluding *S1* and *S2*; Figure 5). For $N_{\min}$, we test $N_{\min} = 5$, 7, and 9 (Figures 1d and 5a, and Figure S2a in Supporting Information S1), and the results suggest a negative correlation between the V_p/V_s estimates and $N_{\min}$. However, the relative differences between the V_p/V_s estimates remain largely unchanged, indicating that the observed spatial pattern is robust. For example, the V_p/V_s estimates of *M2* and *F1* both decrease as $N_{\min}$ increases from 5 to 9, but the estimate of *M2* remains smaller than that of *F1* (Figures 1d and 5a, and S2a in Supporting Information S1). The general decrease of the estimates with increasing $N_{\min}$ may be because a greater $N_{\min}$ reduces the number of measurements with large differential-arrival-time values, which have stronger impacts on the V_p/V_s estimates than the measurements closer to the origin. Including large differential-arrival-time measurements could yield more robust estimates because random errors in these measurements are relatively smaller compared with the measurements themselves. The V_p/V_s estimates for *M1*, *D1*, and *D2* are largely insensitive to the choice of $N_{\min}$ likely due to their more numerous measurements (Figures 1d and 5a, and S2a in Supporting Information S1).

We vary $RMS_{\max}$ from 0.005 to 0.015 s and find that the V_p/V_s estimates are generally insensitive to the choice of the parameter (Figures 1d and 5b, and Figure S2b in Supporting Information S1). For $\tau_{\min}$, we vary its value from 0.025 to 0.075 s and find that the V_p/V_s estimates positively correlate with $\tau_{\min}$, although the spatial variation of the estimates remains the same (Figures 1d and 5c, and S2c in Supporting Information S1). The positive correlation may be because a greater $\tau_{\min}$ tends to select more measurements with large differential travel times, which influences the V_p/V_s estimates in an opposite way to that of $N_{\min}$. This suite of sensitivity tests demonstrates that although the absolute V_p/V_s estimates are affected by the parameters, the resolved spatial variation in V_p/V_s is robust regardless of the preprocessing-parameter choices.

4.2. Temporal Evolution of In-Situ V_p/V_s

The fault patches in the mainshock zone (*M1* and *M2*) and barrier zone (*F1*, *F2*, *D1*, and *D2*) have sufficient measurements to enable us to evaluate the temporal evolution of V_p/V_s in these segments (Figure 6). For each fault patch, we group every 50 consecutive event pairs (after preprocessing) into a time window with a temporal increment of 10 event pairs. This scheme creates nonuniform window lengths but an equal number of measurements for each window, which guarantees that the observed temporal variation is not due to a change in sample size. We then estimate the V_p/V_s for each time window and evaluate its temporal variation. Because the temporal variation of seismicity is very different between different patches, the distribution of time windows also varies greatly between them (Figure 6).

The in-situ V_p/V_s estimates fluctuate at all six fault patches albeit with different degrees. The V_p/V_s estimate of *M1* oscillates within ±3% of the average value and shows no clear trend during the observation period

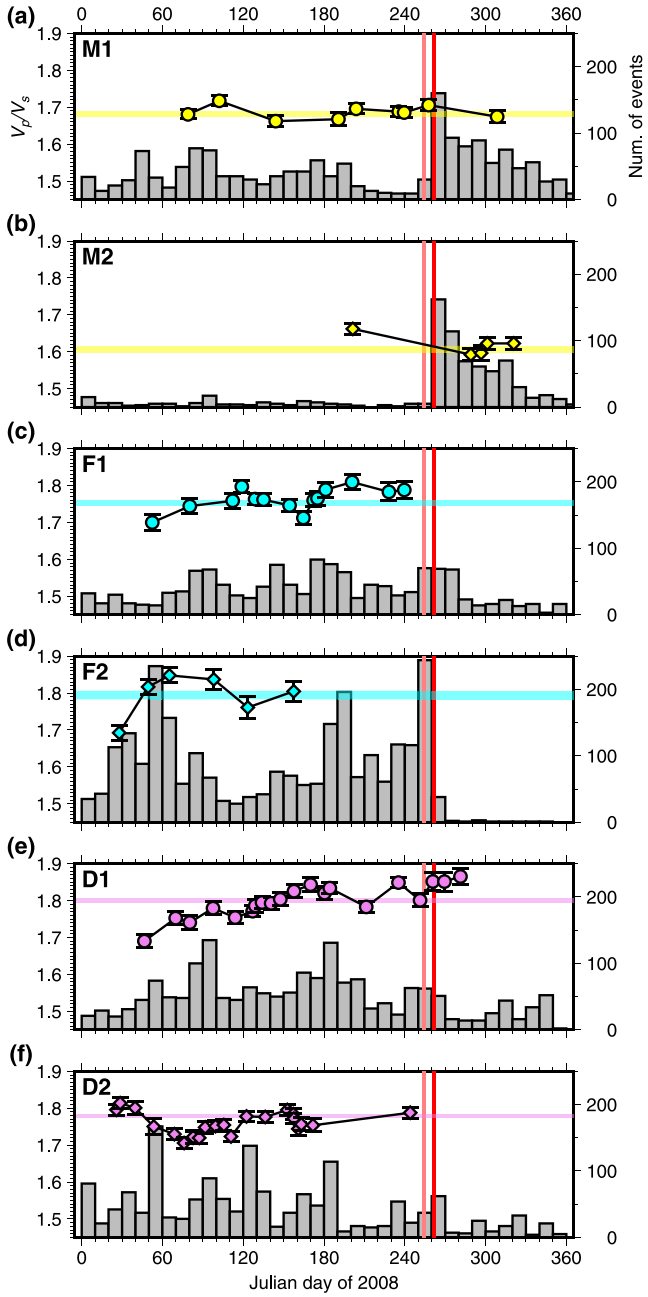

Figure 6. Temporal variations of the in-situ V_p/V_s of (a) *M1*, (b) *M2*, (c) *F1*, (d) *F2*, (e) *D1*, and (f) *D2*. Colored markers: V_p/V_s estimated for each time window plotted at the center of the window. Colored bands: Uncertainty ranges of the V_p/V_s estimated for the whole observation period (Figure 1e). Gray histograms: Event counts with a 10-day bin width. Red vertical line: occurrence of the mainshock. Light red vertical line: occurrences of the three *M*4 foreshocks in the barrier zone.

(Figures 6a and 7c). The V_p/V_s estimate of *M2* appears to have decreased by ~3% after the mainshock, though this change may not be well resolved due to a lack of earthquakes in *M2* before the *M*6 mainshock (Figures 6 and 7c). In contrast, the four barrier-zone patches, *F1*, *F2*, *D1*, and *D2*, show a greater fluctuation with an apparent increasing trend before the *M*6 mainshock (Figures 6c–6e, 7a, and 7b). Hereafter, we will use Julian day (abbreviated as d; number of days since 1 January 2008) to describe the temporal evolution of the in-situ V_p/V_s. For *F1*, the V_p/V_s increased by ~6% between ~60 and ~120 days, dropped by ~5% between ~120 and ~160 days, and increased again by ~5% between ~160 days and the mainshock (Figures 6c and 7b). For *F2*, the V_p/V_s increased by ~9% between ~30 and ~100 days, dropped by ~5% between ~100 and ~120 days, and then increased by ~3% between ~120 and ~160 days (Figures 6d and 7b). Although *F2* had abundant microearthquakes before the mainshock, a smaller percentage of the measurements passed the quality-control procedure compared to other barrier-zone patches, resulting in a lack of measurements in the 100 days immediately before the mainshock (Figure 6d). For *D1*, we observe a nearly-monotonic increase in V_p/V_s before the mainshock with a cumulative change of ~10% (Figures 6e and 7a). In contrast, the V_p/V_s of *D2* dropped by ~5% between ~30 and ~80 days and then gradually increased by ~4% in the remaining time before the mainshock (Figures 6f and 7a).

To examine the robustness of the observed temporal patterns, we also test the effects of the three key preprocessing parameters on the V_p/V_s temporal variations in *M1* and *D1* (Figure S3 in Supporting Information S1). The results show that the trend of an increasing V_p/V_s in *D1* and the lack of temporal changes in *M1* are both robust features regardless of the choice of preprocessing parameters. We notice that including more lower-quality measurements (e.g., in the case of $\tau_{min} = 0.075$ s) would cause more apparent short-time-scale variations, but the long-term trends remain the same. The temporal V_p/V_s changes in the barrier zone (Figures 1b and 6c–6f) may be related to pore-fluid migration or aseismic slip transients as suggested by the intense foreshocks in the barrier zone (Gong & Fan, 2022; McGuire et al., 2012). The observed V_p/V_s increase happened gradually in the 9 months preceding the mainshock and thus is unlikely caused by the largest foreshocks (three ~*M*4 events) occurring within 8 days before the mainshock (light red vertical lines in Figures 6 and 7).

4.3. 3D Synthetic Tests

4.3.1. Validation of Spatial Variation

Lin and Shearer (2007) demonstrated that an in-situ V_p/V_s estimate is free of bias only in idealistic cases where (a) V_p/V_s varies smoothly with depth; (b) the earthquakes form an isotropic distribution; and (c) the stations cover most of the azimuth. Practically, deviations from these conditions may cause biases in the estimates with varying degrees, which depend on the velocity structure, event distribution, and network configuration (Palo et al., 2016). Evaluation of the biases thus needs to be performed on a case-by-case basis. At G3, the barrier zone has a significantly lower V_p compared to the surrounding oceanic lithosphere (Roland et al., 2012), and our results as well as previous studies also suggest a strong along-strike velocity variation (Froment et al., 2014; Guo et al., 2018). Furthermore, the earthquakes are primarily distributed along strike with a narrow strike-normal spread (Figure 1a). Given these conditions, we perform synthetic tests using a suite of 3D velocity models to quantify their effects on the in-situ V_p/V_s estimates.

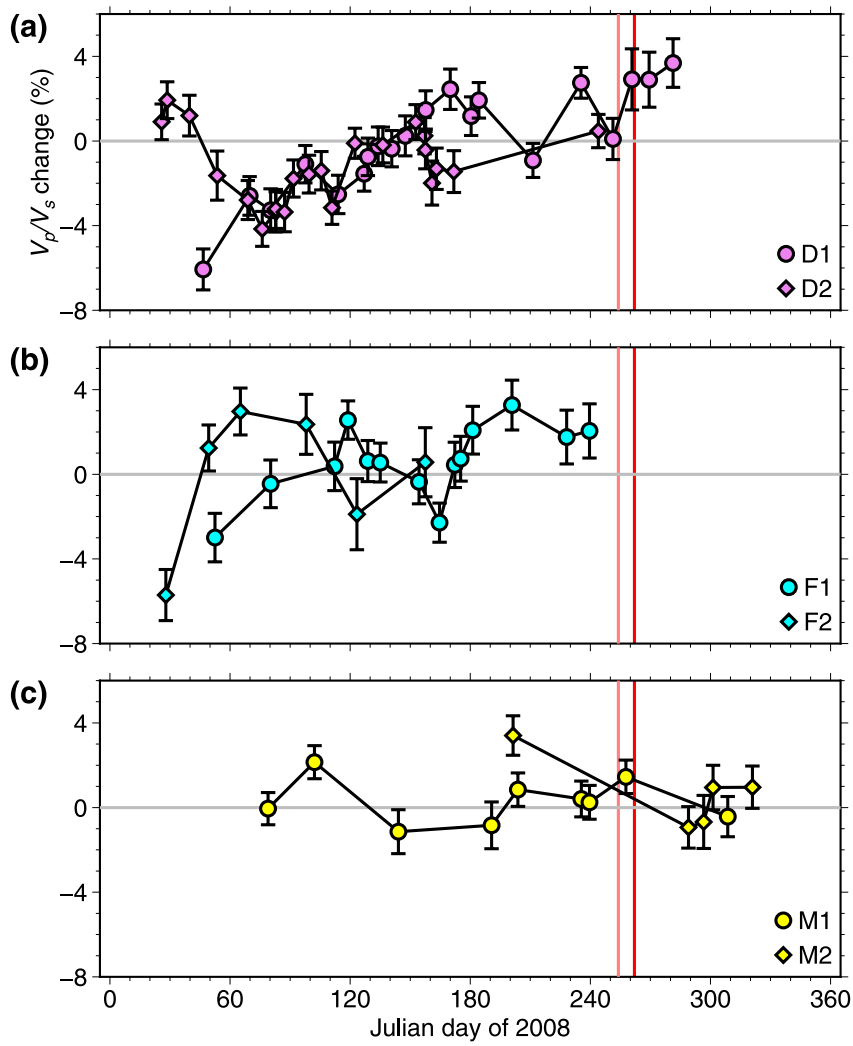

Figure 7. Temporal changes of the V_p/V_s in percentage for (a) *D1* and *D2*, (b) *F1* and *F2*, and (c) *M1* and *M2*. The changes are relative to the V_p/V_s estimated for the whole observation period for the respective fault patches. The vertical lines are the same as in Figure 6.

We test three 3D velocity models (Model 1 to 3) consisting of a vertical fault zone embedded in the oceanic lithosphere (Figures 8 and 9, and Figure S4 in Supporting Information S1). The oceanic lithosphere has the same 1D V_p profile as the one used for locating the earthquakes (Figures 8a and 9a, and Figure S4a in Supporting Information S1; Gong and Fan (2022)). We set the V_p/V_s of the oceanic lithosphere to decrease exponentially from 2.00 at the seafloor to 1.73 at the bottom of the model domain (30 km depth; Figures 8b and 9b, and Figure S4b in Supporting Information S1). This V_p/V_s profile is consistent with those of the oceanic lithosphere derived from active-source experiments (e.g., Spudich & Orcutt, 1980). The fault zone has a uniform, low V_p of 5 km s^{-1} in all the models, which is obtained from Roland et al. (2012) (Figures 8a and 9a, and Figure S4a in Supporting Information S1). The fault zone extends to 10 km depth (Figures 8a and 8b, 9a and 9b, and Figures S4a and S4b in Supporting Information S1) to match the deep seismicity located in *D1* and *D2* (Figures 1b–1d). To assess the effects of the event and station distributions, we use the same station locations and the same earthquakes that are used for estimating the in-situ V_p/V_s (Figures 8a–8c, 9a–9c, and Figures S4a–S4c in Supporting Information S1). We compute synthetic P and S travel times using PyKonal (White et al., 2020), which can efficiently compute travel times and ray paths in 3D models. We then estimate V_p/V_s from the synthetic travel times and compare them with the input values (Figures 8d and 9d, and Figure S4d in Supporting Information S1). The synthetic data are noise-free, which is designed to isolate the effects of 3D velocity structures.

Model 1 has a homogeneous fault zone with a constant V_p/V_s of 1.70 and a width of 5 km (Figures 8a–8c), mimicking the fault-zone width reported in Roland et al. (2012). The results show that the V_p/V_s estimates are

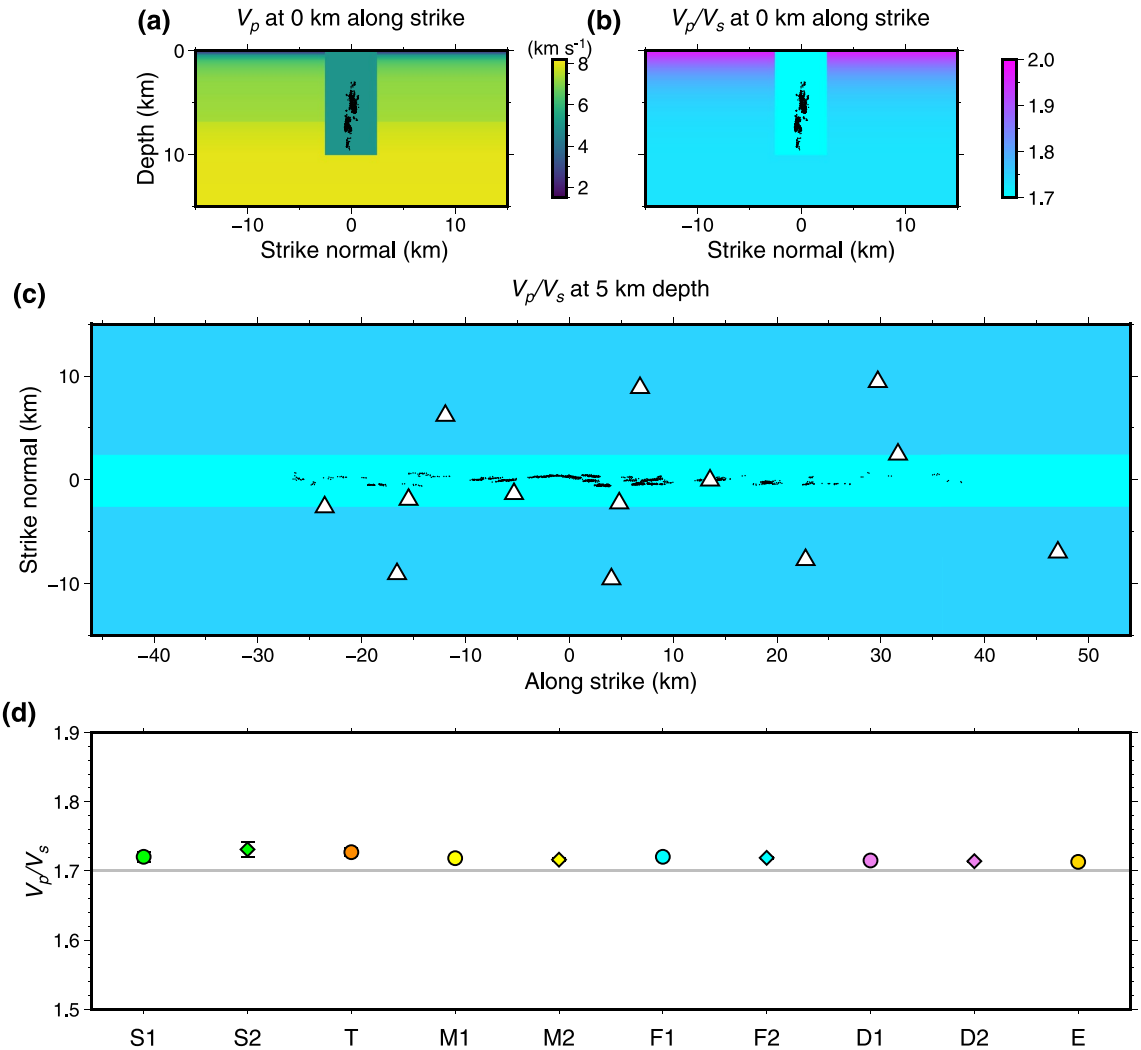

Figure 8. Summary of the 3D synthetic test assuming a homogeneous fault zone (Model 1). Black dots: Events used for the final V_p/V_s estimation. White triangles: Functional stations in Figure 1a (a) Cross section of the V_p model at 0 km along strike. (b) Cross section of the V_p/V_s model at 0 km along strike. (c) Cross section of the V_p/V_s model at the depth of 5 km. (d) Retrieved V_p/V_s of all fault patches (colored markers) compared with the input V_p/V_s of the fault zone (gray line).

close to the input value (Figure 8d). The deviations of the estimated values are smaller than 2% from the input values and show no spatial pattern (Figure 8d). The small deviations are likely due to the smearing effects from the wall rock, which has a higher V_p/V_s at the depths of the events (~1.75; Figures 8b and 8c). These results demonstrate that the observed V_p/V_s contrast between the barrier zone and the mainshock zone is unlikely an artifact due to the source-receiver configuration.

In Model 2, we use a fault zone width of 5 km and assign a low V_p/V_s of 1.70 to the western fault zone, which contains *S1*, *S2*, *T*, *M1*, *M2*, and a high V_p/V_s of 1.80 to the eastern fault zone, which contains *F1*, *F2*, *D1*, *D2*, *E* (Figures 9b and 9c). This V_p/V_s contrast imitates the observed V_p/V_s differences between the mainshock zone and the barrier zone (Figure 1d). The fault zone is kept to have a homogeneous V_p of 5 km s^{-1} (Figure 9a). We find that the contrast in V_p/V_s between the two segments is well recovered (Figure 9d). Similar to Model 1, smearing effects from the wall rock likely cause the V_p/V_s of the western and eastern segments to be slightly overestimated and underestimated, respectively (Figure 9d). These results demonstrate that given the source-receiver configuration, an along-strike V_p/V_s variation similar to the observed one can be resolved with our method.

To assess the resolution of our method, we set Model 3 to have the same along-strike V_p/V_s variation as Model 2 but a fault-zone width of 2 km (Figures S4a–S4c in Supporting Information S1). This value is the lower bound of the fault-zone width reported in Roland et al. (2012). For this case, the estimated V_p/V_s of all fault patches are

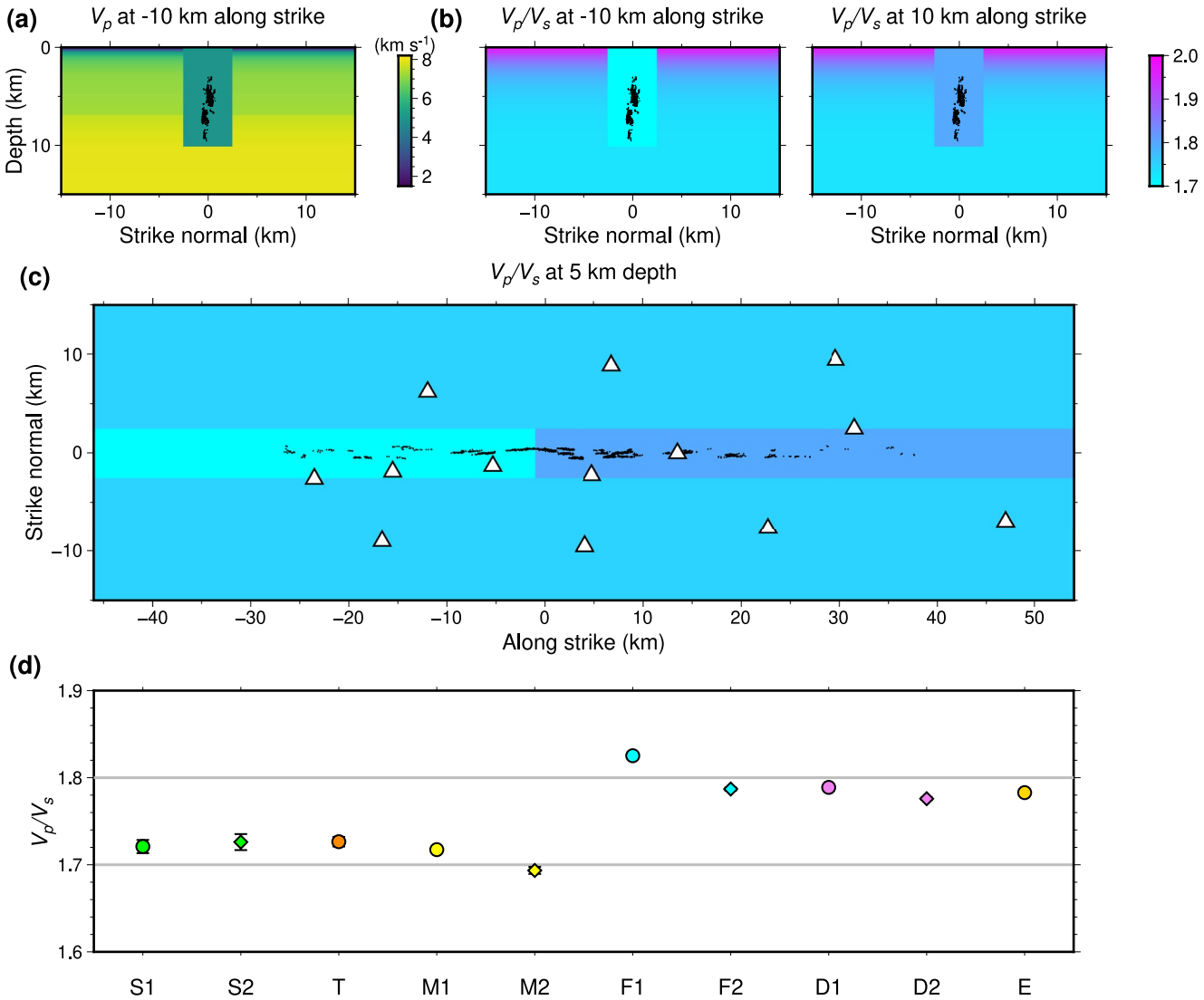

Figure 9. Summary of the 3D synthetic test assuming an along-strike segmented fault zone (Model 2). Legends are the same as in Figure 8. The gray lines in (d) mark the input V_p/V_s of the two segments.

close to 1.75, the V_p/V_s of the wall rock at the event depths, without a clear difference between the two segments (Figure S4d in Supporting Information S1). This example highlights that the smearing effect of the surrounding materials can significantly affect the V_p/V_s estimates of the fault-zone materials when the fault zone is too narrow. We will further discuss the uncertainty caused by 3D velocity structures in Section 5.1.2.

4.3.2. Validation of Temporal Variation

We further design Model 4 and Model 5 to validate the apparent V_p/V_s increase in the barrier zone (*F1*, *F2*, and *D1*). Specifically, we compute the synthetic travel times for the first and the last time windows of the three patches using the true event locations. We then estimate the V_p/V_s using the synthetic data and compare them with the input values. We set Model 4 to have the same velocity structure as Model 1 at both the first and last time windows, that is, Model 4 is time-invariant (Figure 10a). The estimated V_p/V_s show no change over time with values of both time windows within the range of uncertainties found in the case of Model 1 (Figures 8d and 10a). These results demonstrate that the observed temporal change in V_p/V_s in the barrier zone (*F1*, *F2*, and *D1*) is unlikely an artifact caused by a change in event distribution over time. Finally, we use Model 5 to test the resolvability of a temporal change in V_p/V_s similar in size and duration to the observations. Model 5 has the same velocity structure as Model 1 in the first time window and changes to Model 2 in the second window, that is, the V_p/V_s

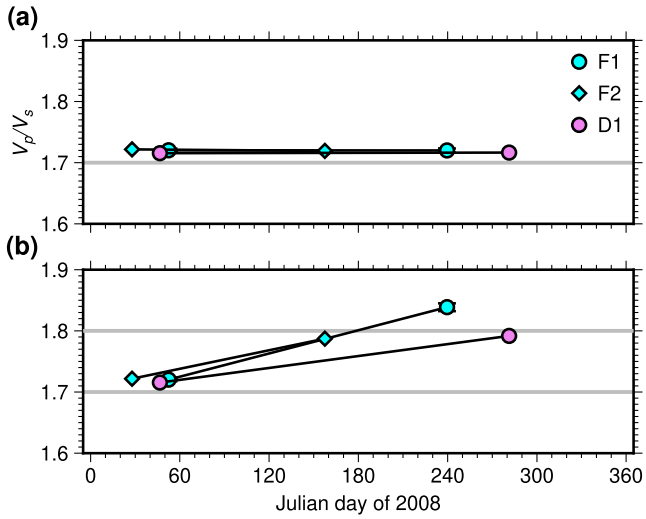

Figure 10. Synthetic tests of the temporal V_p/V_s increase in *F1*, *F2*, and *D1*. (a) Results of using Model 1 as the velocity model at both the first and second time windows. Colored markers: V_p/V_s estimates for the first and second time windows of the three patches of interest. Gray line: Input fault-zone V_p/V_s. (b) Similar to (a), but using Model 1 at the first window and Model 2 at the second window. Gray lines: Input fault-zone V_p/V_s for the two time windows.

of the eastern fault zone increases from 1.70 to 1.80 (Figure 10b). We find that the V_p/V_s changes of all three patches are well recovered with marginal differences from the input values (Figure 10b). These two tests show that the observed V_p/V_s increase in the barrier zone is unlikely an artifact and that a V_p/V_s increase in the barrier zone is resolvable with our method and data.

5. Discussions

5.1. Uncertainty Analyses

We evaluate uncertainties in the in-situ V_p/V_s estimates resulting from two main sources: data noise and model assumptions.

5.1.1. Uncertainty From Noise

The noise in the differential travel-time data has three major components: instrument clock drifts, event-timing errors, and cross-correlation alignment errors. Although the linear time drifts in the OBS data were removed (Gouédard et al., 2014), significant nonlinear time drifts may still be present and could bias the V_p/V_s estimates. To evaluate the potential impacts of instrument clock drifts, we estimate the V_p/V_s for the five fault patches in the mainshock zone and barrier zone (*M1*, *M2*, *F1*, *F2*, *D1*, and *D2*) using different maximum temporal separations between event pairs of 15, 30, 45, and 60 days (Figure 11). The results show that the V_p/V_s estimates decrease slightly (<4%) with increasing maximum event temporal separation, although the relative difference between the patches largely remains the same (Figure 11). Instrument clock drifts introduce the same bias to both the P and S differential travel times, causing the V_p/V_s estimates to converge toward 1, which may explain the negative correlation between the estimated V_p/V_s and the maximum event temporal separation. Given that the V_p/V_s estimated using the preferred maximum event temporal separation (30 days) do not differ significantly from those estimated using a smaller temporal separation limit (15 days; Figure 11), we opt to use 30 days as the limit to maximize the number of measurements and conclude that our results are unlikely biased by instrument clock drifts.

In theory, event-timing errors can be estimated and removed from the data by estimating and removing the intercept terms for individual event pairs. However, other types of noise, especially cross-correlation alignment errors, can complicate corrections for such errors in reality. As the first step of the quality-control process, removing differential travel times with low cross-correlation values (<0.6; Figure 3) cannot fully eliminate cross-correlation measurement errors, which is likely due to misalignment between different phases (e.g., P and S; Figure S5 in Supporting Information S1). Microearthquakes typically have short body wave pulses, and bandpass-filtered P and S waves may have similar waveforms. For example, aligning a P phase with the associated S phase will yield an erroneous differential travel time but a high cross-correlation value, causing outliers in the measurements (Figure 2a). The linearity step in the preprocessing procedure is designed to further eliminate these outliers and simultaneously remove the event-timing errors (Figures 3 and 4).

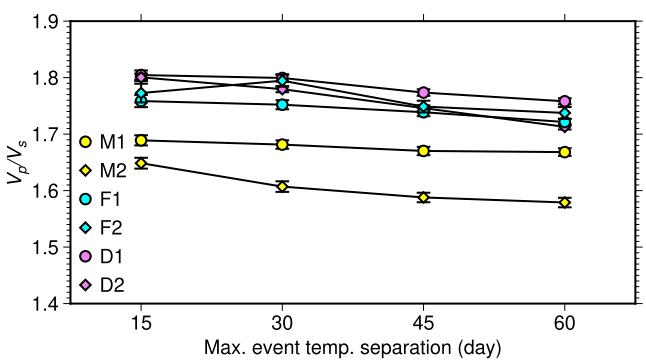

Figure 11. Effects of maximum temporal separation of event pairs on the V_p/V_s estimates for six fault patches. Colored markers: V_p/V_s of different fault patches. Legends are similar to those of Figure 6.

Since the preprocessing procedure removes the majority of the measurements (Figure 2), a reasonable concern is if this procedure could bias the V_p/V_s estimates. To evaluate this possibility, we generate differential P and S arrival times assuming a V_p/V_s of 2.00, an extreme value for rocks, and add synthetic event-timing errors, Gaussian random noise, and outliers step by step to generate three sets of synthetic data (Figure 12). The event-timing errors and Gaussian noise are randomly generated from Gaussian distributions with a zero mean and standard deviations of 0.02 and 0.01 s, respectively, and the outliers are simulated by contaminating 1% of the P and S differential travel times with random noise generated from a uniform distribution between −0.2 and 0.2 s. We then apply the preprocessing and robust slope estimation procedures to these synthetic data and compare the estimated slopes with the input

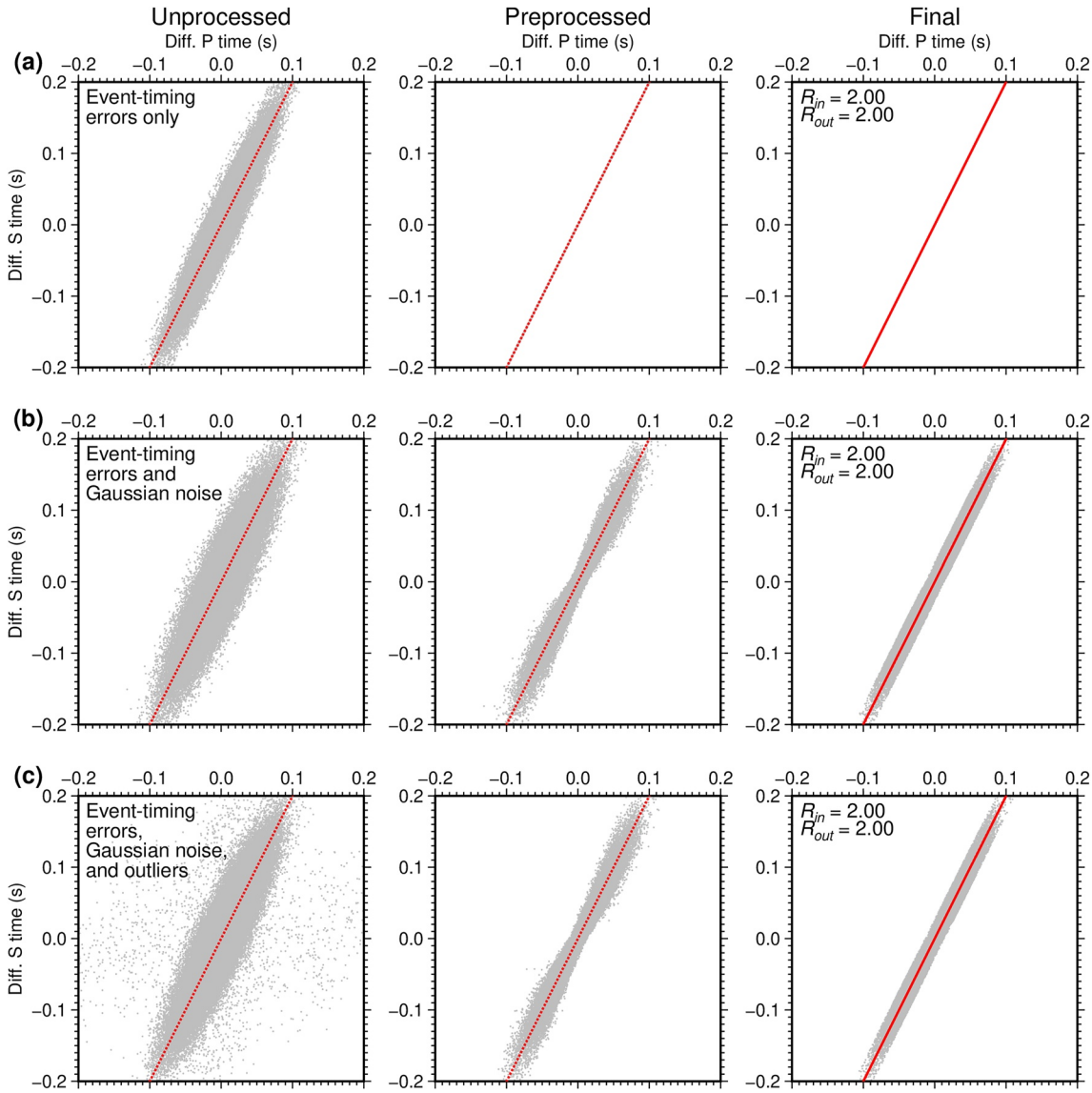

Figure 12. Synthetic tests of the effects of the preprocessing and robust-slope-estimation procedures. Dotted and solid red lines: Models with the true slope (2.00) and the estimated slopes, respectively. The three columns from left to right show input data points, the remaining data points after preprocessing, and the data points used for the final slope estimation, respectively. (a) Input data with only event-timing errors. (b) Input data with event-timing errors and Gaussian noise. (c) Input data with event-timing errors, Gaussian noise, and outliers.

value (Figure 12). The results show that in all three cases, the estimated slopes match the input slope. We also perform the same test on differential travel times generated assuming a V_p/V_s of 1.30, another extreme value for rocks, and find that the results also agree with the input slopes (Figure S6 in Supporting Information S1). These tests demonstrate that the preprocessing procedure does not bias the V_p/V_s estimates.

Common methods for estimating the uncertainty of in-situ V_p/V_s include the bootstrap and jackknife methods (e.g., Bloch et al., 2018; Lin & Shearer, 2007). These methods quantify the coherency of a given set of differential travel times. However, the uncertainty given by bootstrap or jackknife sampling is likely an underestimate because it does not account for the uncertainty associated with the data-selection procedure (Figure 2). Therefore, in addition to estimating the uncertainty by resampling the dataset, we also performed sensitivity tests on $N_{\min}$, $RMS_{\max}$, and $\tau_{\min}$, three key parameters of the preprocessing procedure, to evaluate their effects on the V_p/V_s estimates. The results show that the difference in V_p/V_s between the barrier zone and the mainshock zone is a robust feature regardless of parameter choice (Figure 5).

5.1.2. Uncertainty From Model Assumptions

The in-situ V_p/V_s method implicitly assumes that the P and S waves from an event pair share the same ray path (Lin & Shearer, 2007), which is inaccurate in regions with strong 3D variations in V_p/V_s. We thus used realistic 3D velocity models to evaluate their effects on the V_p/V_s estimates (Figures 8 and 9, and Figure S4 in Supporting Information S1). We show that the V_p/V_s estimates of the fault zone can be biased toward the V_p/V_s of the wall rock (smearing effects) and that the degree of bias depends on the width of the fault zone (Figures 8 and 9, and Figure S4 in Supporting Information S1). The smearing effect is significant in the case of a 2-km wide fault zone (Figure S4 in Supporting Information S1) probably because the width of the V_p/V_s anomaly (2 km) has the same order of magnitude as the maximum event spatial separation (2 km), which causes a significant portion of the differential path between the two events to be outside the V_p/V_s anomaly. Using event pairs with a smaller spatial separation could reduce the smearing effects and increase the spatial resolution at a cost of decreasing the range of differential times (τ), which may cause less reliable slope and intercept estimates. Therefore, the choice of maximum inter-event separation likely controls the trade-off between estimation precision and accuracy. In addition, network configuration is also a key factor in determining the resolution, with a dense and uniform station coverage likely producing more accurate estimates (e.g., Lin & Shearer, 2007).

The synthetic tests show that we can reliably resolve the relative differences in V_p/V_s between different fault segments and time windows. The identified V_p/V_s contrast between the barrier zone and the mainshock zone is likely a true feature, although the absolute value of the contrast may have been underestimated. Similar findings were reported in Bloch et al. (2018) that the in-situ V_p/V_s method is unlikely to produce "false positives" of anomalous values but may be susceptible to "false negatives." Although our synthetic tests show that the in-situ V_p/V_s method also suffers smearing effects similar to tomography methods, it can still resolve sharp boundaries in V_p/V_s ratio between different earthquake source regions such as the one between M2 and F1, which is often challenging for tomography methods to resolve.

Encouragingly, our results suggest that in-situ V_p/V_s could be reliably estimated without the requirement of isotropic event distributions (the events on G3 are mostly distributed along sub-vertical planes; Figures 1b and 1e). This finding suggests a potentially broader application of the method than previously thought, which includes fault zones with planar earthquake distributions. In addition, the relatively uniform station azimuthal coverage at G3 (Figure 1b) likely also contributed to the success of the method at G3. Therefore, the method will likely produce reliable results in cases where events are distributed along sub-vertical planes (e.g., strike-slip fault zones) and the station azimuthal coverage is adequate. Nonetheless, we still recommend performing rigorous synthetic tests using 3D velocity models as demonstrated in our example whenever the method is applied, especially given that efficient 3D ray-tracing codes (e.g., PyKonal) are readily available nowadays.

5.2. Comparison With Previous Tomography Results

The tomography models of Guo et al. (2018) show a strong lateral variation in velocities in the G3 fault zone. The tomography models, including a V_p/V_s model, are obtained using the same OBS waveform data but a different earthquake catalog (Gong & Fan, 2022; Guo et al., 2018). The V_p/V_s model of Guo et al. (2018) suggests a greater range of V_p/V_s variation (~1.5–2.1) than our results (~1.6–1.8; Figure S7 in Supporting Information S1). Both studies agree qualitatively on the high V_p/V_s in *F2* and the low V_p/V_s in *T*, *M1*, and *M2* (Figure S7 in Supporting Information S1). In contrast, Guo et al. (2018) did not observe high V_p/V_s in *F1*, *D1*, and *D2* as shown by our results (Figure S7 in Supporting Information S1). The comparison in *E* may not be meaningful because both models have low resolutions in the region due to the lack of events. The tomography model shows a high V_p/V_s above ~4 km depth in the transition zone (distance ranges −30 to −13 km along strike) and barrier zone (~−7–5 km along strike), which are not resolved in our results due to a lack of seismicity there (Figure S7 in Supporting Information S1).

The apparent differences between our results and those from Guo et al. (2018) may be due to the differences in sensitivity between our method and the tomographic-inversion approach used in Guo et al. (2018). Our method directly estimates the V_p/V_s in a compact earthquake cluster by solving an over-determined problem of fitting a line to the differential travel times, which is likely to yield a robust result. The small footprints of earthquake clusters also provide a high spatial resolution. In contrast, Guo et al. (2018) used differential travel times to solve for the V_p/V_s on a mesh of dense grid points in the volume occupied by their event pairs. Although such a method may

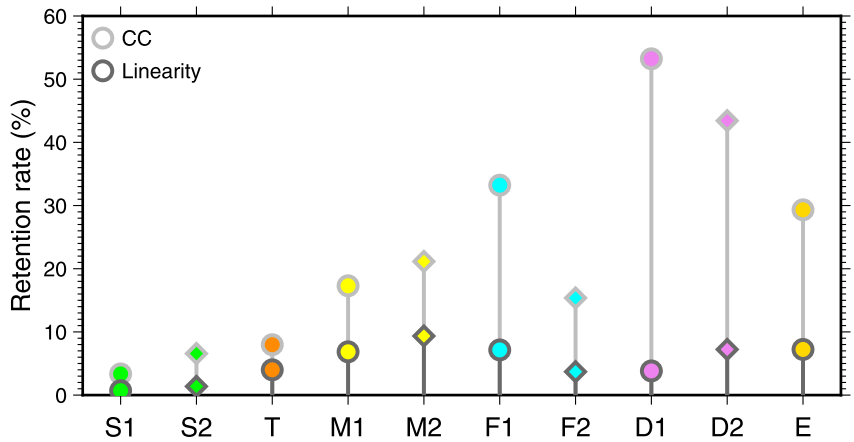

Figure 13. Data retention rates for all fault patches (labeled on the horizontal axis). The rates for the CC step and the linearity step are outlined in light and dark gray, respectively.

offer a higher spatial resolution, the ill-conditioned problem requires smoothing and regularization to stabilize the inversion (Guo et al., 2018). The models of Guo et al. (2018) may provide constraints on the material properties of the shallow part of the barrier zone where earthquakes are sparse. The collective observations of both studies suggest that the V_p/V_s in the entire barrier zone is greater than that in the mainshock zone, consistent with possible sea-water infiltration down to the upper mantle in the barrier zone, which causes the deep seismicity in *D1* and *D2* (McGuire et al., 2012).

5.3. Physical State of G3 Fault Zone

5.3.1. Fault-Zone Structural Complexity

The fraction of the measurements passing the preprocessing procedure, defined as the retention rate, may offer insights into the structural complexity of the fault zone. In the CC step, *D1* and *D2* have high retention rates of 40%–50%; *M1*, *M2*, *F1*, *F2*, and *E* have intermediate retention rates of 15%–35%; and *S1*, *S2*, and *T* have low retention rates of <10% (markers with light-gray edges in Figure 13). The linearity-step retention rates generally correlate with the CC-step retention rates except for *D1* and *D2*, and the linearity-step retention rates are significantly lower (<10%; markers with dark-gray edges in Figure 13), which is partly due to the relatively low cross-correlation-coefficient threshold that we use. A higher cross-correlation-coefficient threshold will likely decrease the CC-step retention rate while increasing the linearity-step retention rate. The retained events in *F2* are mostly located in the deep part of the fault patch (Figure 1d), suggesting a possible difference between the shallow and deep parts of *F2*.

Since we measure differential travel times using waveform cross correlation instead of automatic phase picks, the data retention rate of the CC step is a proxy of the waveform similarity between nearby events in each fault patch. A reduced waveform similarity can be caused by a higher degree of heterogeneity in velocity structure or stress field (Trugman et al., 2020). The data retention rate of the linearity step reflects how well the differential travel times of individual event pairs follow a linear model. A low linearity-step retention rate may be due to noisier differential-travel-time measurements or their general deviation from a linear model. The former may be due to incoherent waveforms, similar to the possible cause of a low CC-step retention rate, and the latter may be due to a heterogeneous velocity structure within the event cluster, which is beyond the resolution of our method. In summary, the retention rates of both steps likely reflect complexities in the fault zone, and their spatial variation suggests various degrees of complexities in different fault patches. Particularly, the low retention rate of F2 might be due to its high degree of fracturing, especially in its shallow portion (Figure 13), which could have enabled hydrothermal circulation to produce a highly heterogeneous velocity structure. Alternatively, some fractures in the barrier zone may be sealed by minerals, which would reduce the fault zone permeability. Either way, the barrier zone is likely saturated with fluid, which could have repeatedly stopped the *M6* ruptures on the adjacent fault segments through dilatancy strengthening (Liu et al., 2020).

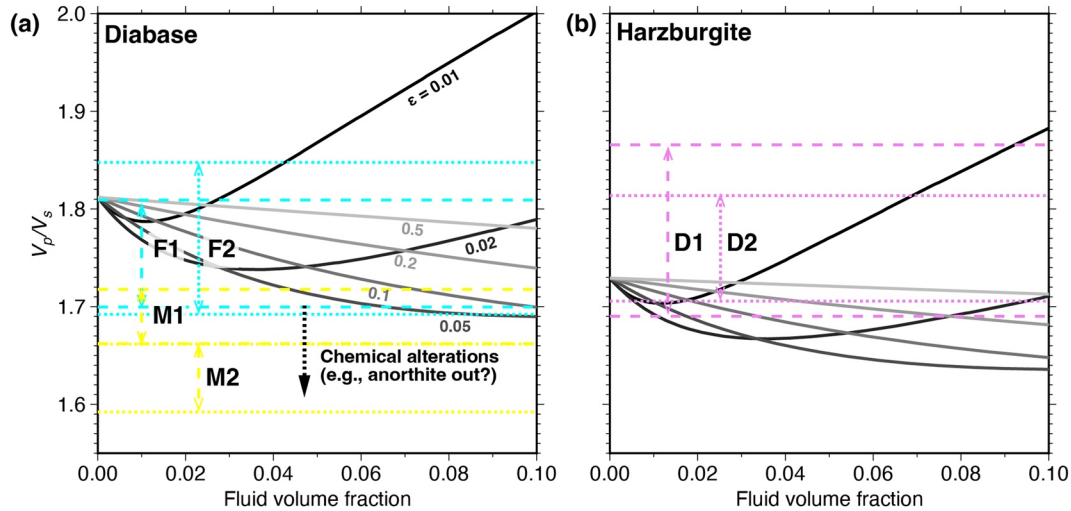

Figure 14. Idealized physical models of effective V_p/V_s of porous rocks for a rock matrix of (a) diabase (Alt et al., 1993) and (b) harzburgite (Lippard, 1986). Black to light-gray curves: Models colored by their pore aspect ratios (ϵ; labeled on the side). Colored dashed and dotted lines: Ranges of the V_p/V_s estimates for the six patches in the mainshock zone (*M1* and *M2*) and the barrier zone (*F1*, *F2*, *D1*, and *D2*). Bold dotted arrow in (a): Potential V_p/V_s decreases due to chemical alterations of the rock matrix, for example, consumption of anorthite.

5.3.2. Physical Models of Fluid-Saturated Rocks

Variations of V_p/V_s in the oceanic lithosphere are often caused by pore fluids (e.g., Barclay et al., 2001; Bloch et al., 2018; Spudich & Orcutt, 1980). Fluid fraction, pore pressure, and pore geometry can all influence the V_p/V_s of water-saturated rocks (e.g., Christensen, 1984; Lin & Shearer, 2009; Shearer, 1988). To investigate the physical causes of the observed in-situ V_p/V_s, we examine the effects of fluid fraction and pore geometry by building idealized porous-medium models and comparing their predictions with the observations. We also discuss the possible role of fluid pressure in causing the temporal variation of the observed V_p/V_s.

In our idealized models, we assume an intact rock matrix with randomly oriented spheroidal pores filled with water, which is characterized by the fluid volume fraction ϕ ($0 < \phi < 1$) and the aspect ratio of the spheroidal pores ϵ ($0 < \epsilon < 1$). For each combination of ϕ and ϵ, we follow Berryman (1980) to construct a self-consistent model to compute the effective V_p/V_s of the medium. Our model requires the elastic parameters and densities of the rock matrix and water. For the rock matrix, we choose two representative rock types for the oceanic crust and upper mantle, namely diabase (Alt et al., 1993) and harzburgite (Lippard, 1986). Their physical properties are adjusted to a temperature and pressure condition of 600 °C and 150 MPa following Abers and Hacker (2016) (hereafter, the physical properties mentioned are all for 600 °C and 150 MPa unless specified otherwise). We obtain the bulk modulus and density of high-temperature-and-pressure water from the specific volume and entropy data in Tödheide (1972). The physical properties of the rock matrices and water at the assumed temperature and pressure are summarized in Table S2 in Supporting Information S2.

We explore the effective V_p/V_s of porous rocks as functions of fluid volume fraction in the range of 0–0.1, assuming different pore aspect ratios for both diabase and harzburgite (Figure 14). The volume-fraction range is derived from Roland et al. (2012), which suggested that the barrier zone has a porosity of ~8%. We find that in the case of a small pore aspect ratio ($\epsilon < 0.02$; thin cracks), the effective V_p/V_s first decreases then increases with increasing fluid volume fraction, whereas in the case of a large pore aspect ratio ($\epsilon > 0.02$; thick cracks), the effective V_p/V_s decreases with increasing fluid fraction (Figure 14). Our results are consistent with the predictions of similar models from previous studies (e.g., Shearer, 1988). The effective V_p/V_s of the diabase model and the harzburgite model show the same relation with fluid fraction and pore aspect ratio except that the former has a greater value than the latter due to a greater V_p/V_s for intact diabase (1.81) than intact harzburgite (1.73; Figure 14).

5.3.3. Comparison Between In-Situ V_p/V_s and Physical-Model Predictions

We compare the V_p/V_s estimates for *F1*, *F2*, *M1*, and *M2* with the predictions of the diabase model because these patches are located in the crust and compare the estimates for *D1* and *D2* with the predictions of the harzburgite

model because they are likely located in the upper mantle (Figure 14). The V_p/V_s estimates of the fault patches fluctuated during the observation period (Figures 6 and 7), which may reflect changes in fluid fraction and pore aspect ratio. We thus use the minimum and maximum V_p/V_s estimates as the reference values for each fault patch and compare them with the predictions of the physical models (Figure 14). For *F1* and *F2*, their minimum V_p/V_s are close to the lower bound of all models and are only consistent with the model with $\epsilon = \sim 0.05$ and $\phi = \sim 0.08$. The maximum V_p/V_s of the two fault patches are close to the V_p/V_s of intact diabase and can be explained by models with a wide range of ϵ and ϕ (Figure 14a). For the mantle patches, the minimum V_p/V_s of *D1* and *D2* are consistent with a wide range of ϕ and ϵ, whereas their maximum values can only be explained by models with a high fluid volume fraction ($\phi > 0.06$) and a small pore aspect ratio ($\epsilon < 0.02$; Figure 14b).

Our V_p/V_s estimates for the barrier zone can generally be explained by porous-medium models with a reasonable fluid volume fraction, consistent with other geophysical evidence (Roland et al., 2012). However, the fluid volume fraction cannot be independently determined due to its coupled effects with pore geometry, which is largely unknown (e.g., pore aspect ratio; Figure 14). Nonetheless, the fluid fraction and pore geometry of the G3 fault zone can be independently constrained by searching for parameter combinations that match both the V_p and V_p/V_s or by incorporating electromagnetic observations, which are also sensitive to pore fluids (e.g., Naif et al., 2015; Takei, 2002).

Intriguingly, the V_p/V_s ranges of *M1* and *M2* are below the lower bound of all models (Figure 14a). These low values thus require physical mechanisms other than pore fluids (Figure 14a). The thermal structure of oceanic transform faults varies gradually along strike (Behn et al., 2007; Roland et al., 2010) and thus is unlikely the cause of the sharp V_p/V_s contrast between the mainshock zone and the barrier zone (Figure 1e). Furthermore, neither diabase nor harzburgite shows a significant change in V_p/V_s within the possible temperature range (Figure S8 in Supporting Information S1; Abers & Hacker, 2016). In contrast, chemical alteration may strongly affect the V_p/V_s of the fault-zone materials. However, Roland et al. (2012) ruled out the presence of a significant amount of serpentine in the G3 barrier zone based on gravity measurements. Therefore, we speculate that other metamorphic minerals from reactions between the basaltic crustal rocks and seawater may have caused the low V_p/V_s of *M1* and *M2*. Specifically, low-grade metamorphic reactions could transfer anorthite in basaltic rocks into minerals with lower V_p/V_p ratios, such as zeolite (1.77), prehnite (1.73), and epidote (1.63) (Best & Myron, 2003). Such processes would systematically reduce the V_p/V_p ratios of *M1* and *M2*, effectively shifting the curves in Figure 14 downward to match the observations for *M1* and *M2* (Figure 14a). In this case, the sharp contrast in V_p/V_s between the mainshock zone and the barrier zone (Figure 1e) could be due to a combined effect of pore fluids and chemical alteration. These inferences of fault-zone material properties will benefit from further petrological and petrophysical investigations on the materials in the Gofar fault zone.

The temporal evolution of the V_p/V_s in the barrier zone (*F1*, *F2*, *D1,* and *D2*) within a few months before the mainshock is unlikely due to a change in mineral composition because metamorphic reactions occur much more slowly (Figures 6c–6f). Therefore, these temporal changes in V_p/V_s are likely due to perturbations of pore fluids. The idealized porous-medium models suggest that a decrease in pore aspect ratio (i.e., thick cracks transitioning into thin cracks) and an increase in fluid fraction can cause an increase in V_p/V_s, which may explain the 9-month V_p/V_s increase observed for *F1*, *F2*, *D1*, and *D2* (Figure 14). The temporal evolution of the fluid fraction and pore geometry in the barrier zone may also reflect variation in pore pressure resulting from aseismic slip transients as predicted by numerical simulations including dilatancy effects (Liu et al., 2020), which is currently challenging to observe due to the absence of seafloor geodetic instrumentation. Our method offers an alternative way to constrain aseismic slip transits in water-infiltrated fault zones, although more work about the relationship between fluid volume fraction, pore geometry, and pore pressure is needed to bridge the gap between the observed temporal variation of in-situ V_p/V_s and the dynamic evolution of the fault-zone materials.

6. Conclusions

We design a purpose-driven approach to estimate the in-situ V_p/V_s using the ocean-bottom-seismometer data collected at the westernmost Gofar transform fault. We find that the fault zone material has a clear along-strike variation in V_p/V_s, with the eastern segment, which includes the barrier zone, having a moderate V_p/V_s of 1.75–1.80 and the western segment, which includes the down-dip edge of the 2008 *M*6 earthquake, having a low V_p/V_s of 1.61–1.69. This spatial variation may be caused by differences in pore fluids and chemical alteration. We also observe a 9-month V_p/V_s increase in the barrier zone, which may be caused by a combined effect of an

increasing number of thin cracks and increasing fluid fraction. These changes may reflect pore-pressure perturbations resulting from aseismic slip transients. Our results suggest that the in-situ V_p/V_s method is a useful tool for monitoring the physical state of fault-zone materials. We also highlight the importance of rigorous synthetic tests using realistic 3D velocity models in future applications to examine possible estimation biases due to limits in assumptions and observations.

Data Availability Statement

The waveform data are downloaded from the Data Management Center (DMC) of the Incorporated Research Institutions for Seismology (IRIS) under the network code ZD. The metadata of the network can be accessed at https://ds.iris.edu/mda/ZD/?starttime=2007-01-01T00:00:00&endtime=2009-12-31T23:59:59. The earthquake catalog is from Gong and Fan (2022) and is archived in Marine Geoscience Data System (DOI: 10.26022/IEDA/331024). The bathymetry data are obtained from https://www.ngdc.noaa.gov/maps/autogrid/. The SciPy TLS package is described at https://docs.scipy.org/doc/scipy/reference/odr.html. Pykonal is available at https://github.com/malcolmw/pykonal.

Acknowledgments
We thank the Editor Rachel Abercrombie, Associate Editor, Dr. Wasja Bloch, and an anonymous reviewer for their thoughtful and constructive reviews of our paper. T.L. is supported by National Science Foundation (NSF) grants EAR 1829601 and EAR 2123529 and a Green Postdoctoral Scholarship. J.G. and W.F. are supported by NSF grants OCE-1833279 and EAR-2143413. G.L. is supported by EAR-2022429. The ocean bottom seismometer instruments were provided by the Ocean Bottom Seismograph Instrument Center (OBSIC). OBSIC data are archived at the IRIS Data Management Center, which is funded by the National Science Foundation's Seismological Facilities for the Advancement of Geoscience (SAGE) Award under Cooperative Support Agreement EAR-1851048. We thank Malcolm White for helping us use PyKonal and Geoffrey Abers for helping us calculate the physical properties of rocks at high temperatures and pressures. We thank Hao Guo for sharing the data file of the model in his paper. We thank Jeffrey McGuire, John Collins, and the rest of the 2008 Quebrada-Discovery-Gofar experiment team for collecting and archiving the data. We also thank Wenlu Zhu for the insightful discussions.

References

Abers, G. A., & Hacker, B. R. (2016). A MATLAB toolbox and excel workbook for calculating the densities, seismic wave speeds, and major element composition of minerals and rocks at pressure and temperature. *Geochemistry, Geophysics, Geosystems*, *17*(2), 616–624. https://doi.org/10.1002/2015gc006171

Alt, J. C., Kinoshita, H., Stokking, L., Allerton, S., Bach, W., Becker, K., et al. (1993). *Ocean Drilling Program Leg 148, Preliminary report Hole 504B*. Ocean Drilling Program.

Bachura, M., & Fischer, T. (2016). Detailed velocity ratio mapping during the aftershock sequence as a tool to monitor the fluid activity within the fault plane. *Earth and Planetary Science Letters*, *453*, 215–222. https://doi.org/10.1016/j.epsl.2016.08.017

Barclay, A. H., Toomey, D. R., & Solomon, S. C. (2001). Microearthquake characteristics and crustal V_p/V_s structure at the Mid-Atlantic Ridge, 35 n. *Journal of Geophysical Research*, *106*(B2), 2017–2034. https://doi.org/10.1029/2000jb900371

Behn, M. D., Boettcher, M. S., & Hirth, G. (2007). Thermal structure of oceanic transform faults. *Geology*, *35*(4), 307–310. https://doi.org/10.1130/g23112a.1

Berryman, J. G. (1980). Long-wavelength propagation in composite elastic media II. Ellipsoidal inclusions. *Journal of the Acoustical Society of America*, *68*(6), 1820–1831. https://doi.org/10.1121/1.385172

Best, G., & Myron. (2003). Mineral Assemblages in Mafic Protoliths: A Brief Overview. In *Igneous and Metamorphic Petrology* (2nd ed., p. 587). Blackwell Science Ltd.

Bloch, W., John, T., Kummerow, J., Salazar, P., Krüger, O. S., & Shapiro, S. A. (2018). Watching Dehydration: Seismic Indication for Transient Fluid Pathways in the Oceanic Mantle of the Subducting Nazca Slab. *Geochemistry, Geophysics, Geosystems*, *19*(9), 3189–3207. https://doi.org/10.1029/2018gc007703

Boettcher, M. S., & McGuire, J. J. (2009). Scaling relations for seismic cycles on mid-ocean ridge transform faults. *Geophysical Research Letters*, *36*(21), L21301. https://doi.org/10.1029/2009gl040115

Christensen, N. I. (1984). Pore pressure and oceanic crustal seismic structure. *Geophysical Journal International*, *79*(2), 411–423. https://doi.org/10.1111/j.1365-246x.1984.tb02232.x

Christensen, N. I. (1996). Poisson's ratio and crustal seismology. *Journal of Geophysical Research*, *101*(B2), 3139–3156. https://doi.org/10.1029/95jb03446

Dahm, T., & Fischer, T. (2014). Velocity ratio variations in the source region of earthquake swarms in NW Bohemia obtained from arrival time double-differences. *Geophysical Journal International*, *196*(2), 957–970. https://doi.org/10.1093/gji/ggt410

Froment, B., McGuire, J., Van der Hilst, R., Gouédard, P., Roland, E., Zhang, H., & Collins, J. (2014). Imaging along-strike variations in mechanical properties of the Go far transform fault, East Pacific Rise. *Journal of Geophysical Research: Solid Earth*, *119*(9), 7175–7194. https://doi.org/10.1002/2014jb011270

Gong, J., & Fan, W. (2022). Seismicity, Fault Architecture, and Slip Mode of the Westernmost Gofar Transform Fault. *Journal of Geophysical Research: Solid Earth*, *127*(11), e2022JB024918. https://doi.org/10.1029/2022jb024918

Gong, J., Fan, W., & Parnell-Turner, R. (2022). Microseismicity Indicates Atypical Small-Scale Plate Rotation at the Quebrada Transform Fault System, East Pacific Rise. *Geophysical Research Letters*, *49*(3), e2021GL097000. https://doi.org/10.1029/2021gl097000

Gouédard, P., Seher, T., McGuire, J. J., Collins, J. A., & Van der Hilst, R. D. (2014). Correction of Ocean-Bottom Seismometer Instrumental Clock Errors Using Ambient Seismic Noise. *Bulletin of the Seismological Society of America*, *104*(3), 1276–1288. https://doi.org/10.1785/0120130157

Guo, H., Zhang, H., & Froment, B. (2018). Structural control on earthquake behaviors revealed by high-resolution V_p/V_s imaging along the Gofar transform fault, East Pacific Rise. *Earth and Planetary Science Letters*, *499*, 243–255. https://doi.org/10.1016/j.epsl.2018.07.037

Lin, G., Amelung, F., Shearer, P. M., & Okubo, P. G. (2015). Location and size of the shallow magma reservoir beneath kīlauea caldera, constraints from near-source V_p/V_s ratios. *Geophysical Research Letters*, *42*(20), 8349–8357. https://doi.org/10.1002/2015gl065802

Lin, G., Peng, Z., & Neves, M. (2022). Comparisons of *in situ* V_p/V_s ratios and seismic characteristics between northern and southern California. *Geophysical Journal International*, *229*(3), 2162–2174. https://doi.org/10.1093/gji/ggac038

Lin, G., & Shearer, P. (2007). Estimating Local V_p/V_s Ratios within Similar Earthquake Clusters. *Bulletin of the Seismological Society of America*, *97*(2), 379–388. https://doi.org/10.1785/0120060115

Lin, G., & Shearer, P. M. (2009). Evidence for water-filled cracks in earthquake source regions. *Geophysical Research Letters*, *36*(17), L17315. https://doi.org/10.1029/2009gl039098

Lin, G., & Shearer, P. M. (2021). Spatiotemporal Variations of Focal Mechanism and In Situ V_p/V_s Ratio During the 2018 Kīlauea Eruption. *Geophysical Research Letters*, *48*(18), e2021GL094636. https://doi.org/10.1029/2021gl094636

Lin, G., Shearer, P. M., & Hauksson, E. (2007). Applying a three-dimensional velocity model, waveform cross correlation, and cluster analysis to locate southern California seismicity from 1981 to 2005. *Journal of Geophysical Research*, *112*(B12), B12309. https://doi.org/10.1029/2007jb004986

Lippard, S. J. (1986). *The Ophiolite of Northern Oman* (Vol. 11, p. 178). Geological Society London Memoir.

Liu, Y., McGuire, J. J., & Behn, M. D. (2020). Aseismic transient slip on the Gofar transform fault, East Pacific Rise. *Proceedings of the National Academy of Sciences*, *117*(19), 10188–10194. https://doi.org/10.1073/pnas.1913625117

McGuire, J. J. (2008). Seismic Cycles and Earthquake Predictability on East Pacific Rise Transform Faults. *Bulletin of the Seismological Society of America*, *98*(3), 1067–1084. https://doi.org/10.1785/0120070154

McGuire, J. J., Boettcher, M. S., & Jordan, T. H. (2005). Foreshock sequences and short-term earthquake predictability on East Pacific Rise transform faults. *Nature*, *434*(7032), 457–461. https://doi.org/10.1038/nature03377

McGuire, J. J., Collins, J. A., Gouédard, P., Roland, E., Lizarralde, D., Boettcher, M. S., & Van Der Hilst, R. D. (2012). Variations in earthquake rupture properties along the Gofar transform fault, East Pacific Rise. *Nature Geoscience*, *5*(5), 336–341. https://doi.org/10.1038/ngeo1454

Naif, S., Key, K., Constable, S., & Evans, R. L. (2015). Water-rich bending faults at the Middle America Trench. *Geochemistry, Geophysics, Geosystems*, *16*(8), 2582–2597. https://doi.org/10.1002/2015gc005927

Palo, M., Tilmann, F., & Schurr, B. (2016). Applicability and Bias of V_p/V_s Estimates by P and S Differential Arrival Times of Spatially Clustered Earthquakes. *Bulletin of the Seismological Society of America*, *106*(3), 1055–1063. https://doi.org/10.1785/0120150300

Roland, E., Behn, M. D., & Hirth, G. (2010). Thermal-mechanical behavior of oceanic transform faults: Implications for the spatial distribution of seismicity. *Geochemistry, Geophysics, Geosystems*, *11*(7). https://doi.org/10.1029/2010gc003034

Roland, E., Lizarralde, D., McGuire, J. J., & Collins, J. A. (2012). Seismic velocity constraints on the material properties that control earthquake behavior at the Quebrada-Discovery-Gofar transform faults, East Pacific Rise. *Journal of Geophysical Research*, *117*(B11). https://doi.org/10.1029/2012jb009422

Shearer, P. M. (1988). Cracked media, Poisson's ratio and the structure of the upper oceanic crust. *Geophysical Journal International*, *92*(2), 357–362. https://doi.org/10.1111/j.1365-246x.1988.tb01149.x

Spudich, P., & Orcutt, J. (1980). Petrology and porosity of an oceanic crustal site: Results from wave form modeling of seismic refraction data. *Journal of Geophysical Research*, *85*(B3), 1409–1433. https://doi.org/10.1029/jb085ib03p01409

Takei, Y. (2002). Effect of pore geometry on V_p/V_s: From equilibrium geometry to crack. *Journal of Geophysical Research*, *107*(B2), ECV-6. https://doi.org/10.1029/2001jb000522

Tödheide, K. (1972). Water at High Temperatures and Pressures. In F. Franks (Ed.), *Water: A Comprehensive Treatise* (Vol. 1, pp. 464–482). Plenum Press. https://doi.org/10.1007/978-1-4684-8334-5_13

Trugman, D. T., Ross, Z. E., & Johnson, P. A. (2020). Imaging Stress and Faulting Complexity Through Earthquake Waveform Similarity. *Geophysical Research Letters*, *47*(1), e2019GL085888. https://doi.org/10.1029/2019gl085888

Van Huffel, S., & Vandewalle, J. (1991). *The total least squares problem: Computational aspects and analysis*. SIAM.

White, M. C., Fang, H., Nakata, N., & Ben-Zion, Y. (2020). Pykonal: A Python Package for Solving the Eikonal Equation in Spherical and Cartesian Coordinates Using the Fast Marching Method. *Seismological Research Letters*, *91*(4), 2378–2389. https://doi.org/10.1785/0220190318

Wolfson-Schwehr, M., Boettcher, M. S., McGuire, J. J., & Collins, J. A. (2014). The relationship between seismicity and fault structure on the Discovery transform fault, East Pacific Rise. *Geochemistry, Geophysics, Geosystems*, *15*(9), 3698–3712. https://doi.org/10.1002/2014gc005445